AGU PUBLICATIONS

JGR

Journal of Geophysical Research: Oceans

RESEARCH ARTICLE

10.1002/2015JC010760

Key Points:
- Super typhoon Haiyan caused extreme flooding on reef coasts
- Wave transformation processes over fringing reefs are numerically reproduced
- Spectral wave characteristics varies with the reef width and beach slope

Supporting Information:
- Supporting Information S1

Correspondence to:
T. Shimozono,
shimozono@coastal.t.u-tokyo.ac.jp

Citation:
Shimozono, T., Y. Tajima, A. B. Kennedy, H. Nobuoka, J. Sasaki, and S. Sato (2015), Combined infragravity wave and sea-swell runup over fringing reefs by super typhoon Haiyan, *J. Geophys. Res. Oceans*, *120*, 4463–4486, doi:10.1002/2015JC010760.

Received 31 JAN 2015
Accepted 26 MAY 2015
Accepted article online 29 MAY 2015
Published online 19 JUN 2015

Combined infragravity wave and sea-swell runup over fringing reefs by super typhoon Haiyan

Takenori Shimozono[1], Yoshimitsu Tajima[1], Andrew B. Kennedy[2], Hisamichi Nobuoka[3], Jun Sasaki[4], and Shinji Sato[1]

[1]Department of Civil Engineering, University of Tokyo, Tokyo, Japan, [2]Department of Civil and Environmental Engineering and Earth Sciences, University of Notre Dame, Notre Dame, Indiana, USA, [3]Department of Urban and Civil Engineering, Ibaraki University, Mito, Japan, [4]Department of Socio-Cultural Environmental Studies, University of Tokyo, Chiba, Japan

Abstract Super typhoon Haiyan struck the Philippines on 8 November 2013, marking one of the strongest typhoons at landfall in recorded history. Extreme storm waves attacked the Pacific coast of Eastern Samar where the violent typhoon first made landfall. Our field survey confirmed that storm overwash heights of 6–14 m above mean sea level were distributed along the southeastern coast and extensive inundation occurred in some coastal villages in spite of natural protection by wide fringing reefs. A wave model based on Boussinesq-type equations is constructed to simulate wave transformation over shallow fringing reefs and validated against existing laboratory data. Wave propagation and runup on the Eastern Samar coast are then reproduced using offshore boundary conditions based on a wave hindcast. The model results suggest that extreme waves on the shore are characterized as a superposition of the infragravity wave and sea-swell components. The balance of the two components is strongly affected by the reef width and beach slope through wave breaking, frictional dissipation, reef-flat resonances, and resonant runup amplification. Therefore, flood characteristics significantly differ from site to site due to a large variation of the two topographic parameters on the hilly coast. Strong coupling of infragravity waves and sea swells produces extreme runup on steep beaches fronted by narrow reefs, whereas the infragravity waves become dominant over wide reefs and they evolve into bores on steep beaches.

1. Introduction

On 8 November 2013, super typhoon Haiyan, which may have been the strongest tropical cyclone to make landfall in recorded history, traversed the central Philippines from the southeast to the northwest, wiping out coastal towns and cities (Figure 1a). The lowest pressure and the maximum 10 min sustained wind speed were estimated at 895 hPa and 230 km h^{-1}, respectively, as it approached the Philippines, by the regional specialized meteorological center (Japan Meteorological Agency). It became one of the deadliest typhoons on record in the country [*Ribera et al*., 2008], killing at least 6300 people. The damage caused by the typhoon was most severe in the city of Tacloban, located at the northeastern tip of Leyte Island where storm surge was significant due to the shallow bathymetry and the funneling shape of the Gulf of Leyte. Field reconnaissance after the event revealed that surge heights reached up to 5–6 m in the inner part of San Pedro Bay located at the northwestern end of the Gulf of Layte, [*Tajima et al*., 2014]. The local amplification of the storm surge was well reproduced by a numerical storm surge model in combination with weather prediction models [*Mori et al*., 2014].

The southeastern coast of Samar Island facing the Pacific Ocean, where the typhoon first made violent landfall, was also heavily devastated. Just off the coast is the Philippine Trench which rapidly descends to a depth of over 8000 m. A majority of the coastline is fronted by shallow fringing reefs with varying widths of some hundreds of meters. High watermarks exceeding 10 m above sea level were confirmed after the event at numerous locations [*Tajima et al*., 2014; *Mas et al*., 2014]. Some coastal towns were inundated to a few hundreds of meters inland and many houses on low-lying areas were washed away. These damages typical to the nature of long wave runup are, however, not considered to have been caused by storm surges since the steep seafloor did not permit growth of the wind setup. Instead, storm waves were extremely high on the Pacific coast near landfall. The remarkably steep bathymetry allowed huge waves to develop and propagate to the reef front. The extensive damages are most likely to have resulted from high wind waves,

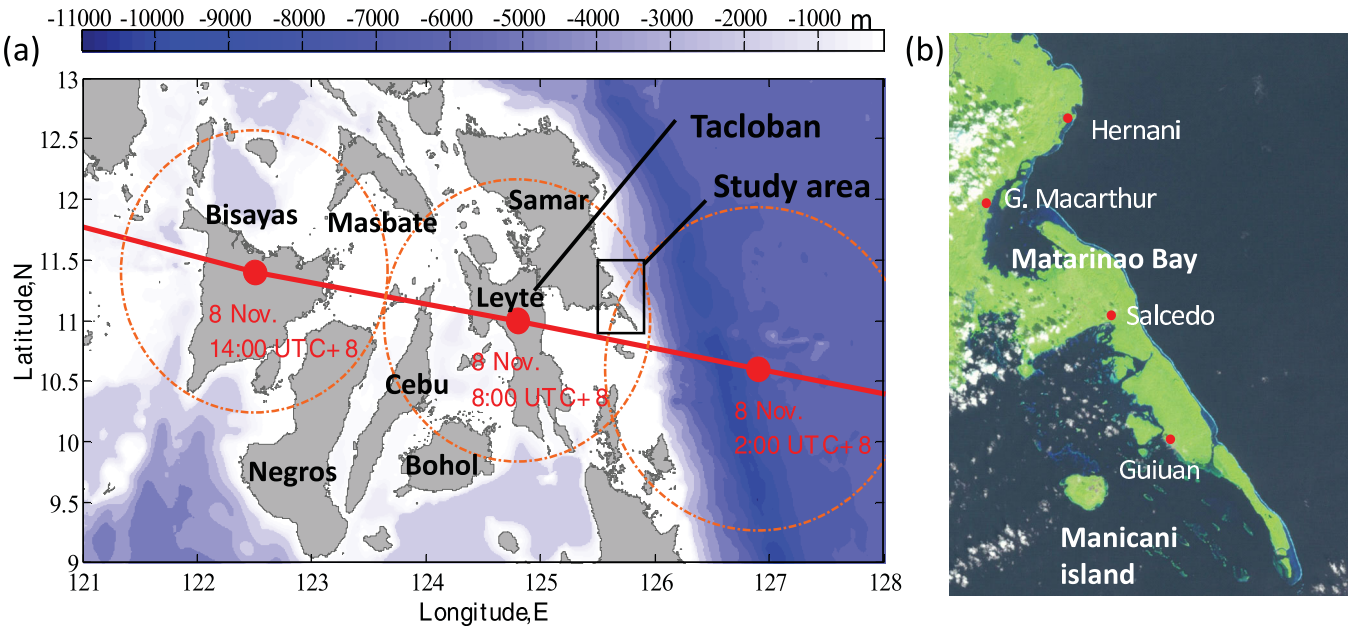

Figure 1. Overview of the study area. (a) Map of the Central Philippines showing the track of the typhoon Haiyan. (b) Satellite image of the southeastern coast of Eastern Samar taken by LANDSAT on 16 December 2001.

especially infragravity waves generated through nonlinear wave transformation over the reef bathymetry. There are numerous field reports on extreme flooding over fringing reefs during coastal storms [*Ogg and Koslow*, 1978; *Nakaza et al*., 1990; *Jaffe and Richmond*, 1993], many of which suggest that infragravity waves play a key role in increasing flood damages.

Coral reefs provide protection for coastal areas by reducing wave energy as shown in numerous studies of wave transformation over reefs. Reef hydrodynamics at different scales were recently well reviewed by *Monismith* [2007]. Incoming waves break at the reef front and lose majority of their energy in the first few wavelengths [*Gourlay*, 1994; *Young*, 1989; *Hardy and Young*, 1996]. Subsequent waves propagate into the shallow reef flat in bore-like form, losing further energy due to bottom friction on the reef surface. The friction factor of coral reefs has been long investigated by many authors in both field and laboratory experiments. Reported values of the friction factor are, in general, 1 order of magnitude larger than those used for sandy beaches [*Gerritsen*, 1980; *Hearn*, 1999; *Lowe et al*., 2005; *Péquignet et al*., 2011]. The rapid decay of wave amplitude produces cross-shore gradients of radiation stress to induce a significant wave setup on the reef. Mean water levels can be raised by 20% of the incident wave height [*Gourlay*, 1996a, 1996b].

The wave transformation over the reef front has another aspect in that energy transfer takes place from a central frequency band of incident waves to a lower-frequency band. As higher harmonics are subject to stronger attenuation, the infragravity spectral band becomes dominant in the nearshore region of the shallow reef flat. Resonant amplification could be excited if a significant amount of wave energy were distributed around the natural frequency of the reef flat. Under normal wave conditions, the reef-flat resonance is not remarkable since the resonance period of the fundamental mode is usually much longer than the mean period of incident waves. However, in an extreme wave climate, a large wave setup on the reef shortens the reef-flat resonance period leading to the resonant amplification of infragravity waves [*Péquignet et al*., 2009]. The enhancement of infragravity waves could be a key process to cause the extensive inundation on the reef coast. However, since most of the existing studies focusing on the dynamics of the reef infragravity waves were conducted under normal wave conditions [e.g., *Lugo-Fernández et al*., 1998; *Pomeroy et al*., 2012], little is known about their characteristics under extreme storm conditions.

The goal of this paper is to elucidate underlying processes leading to extreme runup heights and extensive inundation areas on the southeastern coast of Eastern Samar. We first present results of our field survey to further investigate the wave impacts on the coast, with a focus on obtaining the relationship between overwash heights and adjacent reef widths along the coastline. Next, we develop a numerical model for wave

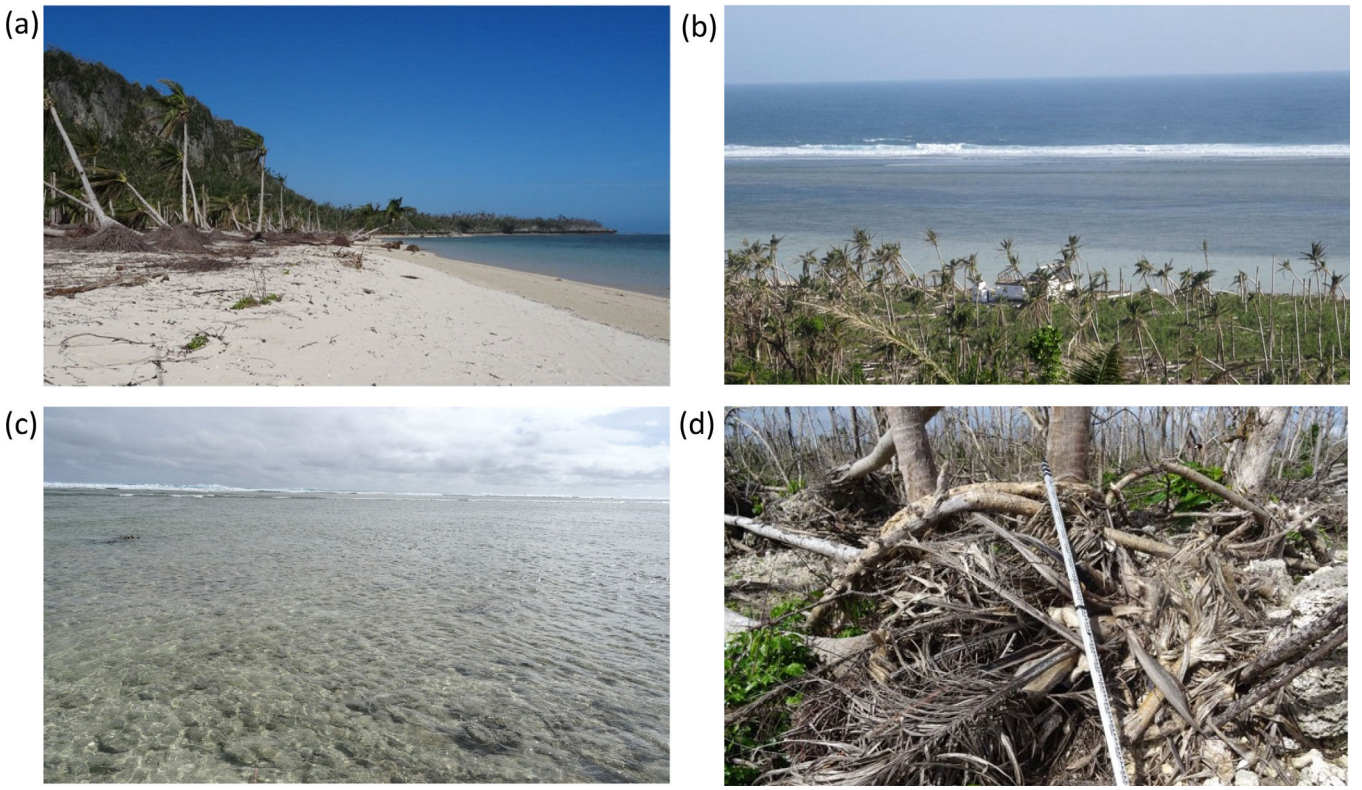

Figure 2. Photographs taken during the field survey in Eastern Samar. (a) Narrow sandy beach backed by a limestone cliff. (b) View of a wide reef flat from the top of a cliff. (c) Reef surface and (d) debris due to storm overwash.

transformation processes over fringing reefs and validate its performance using existing laboratory data. Model input parameters are determined through sensitivity analyses so as to reproduce the field data. Finally, we discuss extreme flood characteristics through model applications.

2. Field Survey

2.1. Survey Area and Methodology

The survey area, indicated by a rectangle in Figure 1a, was chosen to cover the southeastern tip of Samar Island. The choice of the area was made on the basis of the previous report of the quick reconnaissance by *Tajima et al.* [2014], who found evidence indicating high water levels of over 10 m above mean sea level on the central coast. A satellite image of the survey area is shown in Figure 1b. The northern coast around Matarinao Bay develops an irregular coastline with some mangrove swamps, while the southern coast has smooth beaches fronted by reef flats. The coastline consists of a long stretch of narrow sandy beaches with widths rarely exceeding 100 m, interrupted by rocky headlands in places. Coastal plains behind the sandy beaches are covered with dense tropical vegetation and backed by steep limestone hills. Figure 2a shows a typical coastal scene with a sandy beach, palm trees, and a limestone hill behind, photographed after the event. The beach is fronted by shallow fringing reefs of 30–800 m from the shore in most places (Figure 2b). The reef top is almost perfectly level and the water depth is small, 0–1.0 m depending on tidal phase (Figure 2c). Most of the coral reefs in the area are in poor condition and coral diversity is low possibly due to frequent typhoon damage [*Young and Cruz*, 2002]. Thus, the reef surface conditions are similar all along the coastline.

We conducted the field survey along the southeastern coast to investigate the distribution of high water levels reached by typhoon surges and waves, referred to hereafter as the overwash height. The main survey was carried out on 23–25 January 2014, while a small follow-up survey was performed on 8–10 July 2014. Individual survey sites were determined from satellite images to cover the target coastline at an average interval of about 1 min of latitude. At many sites, there was no difficulty in finding clear evidence of high water levels during the typhoon period, including debris wrack lines, scour around roots of standing trees,

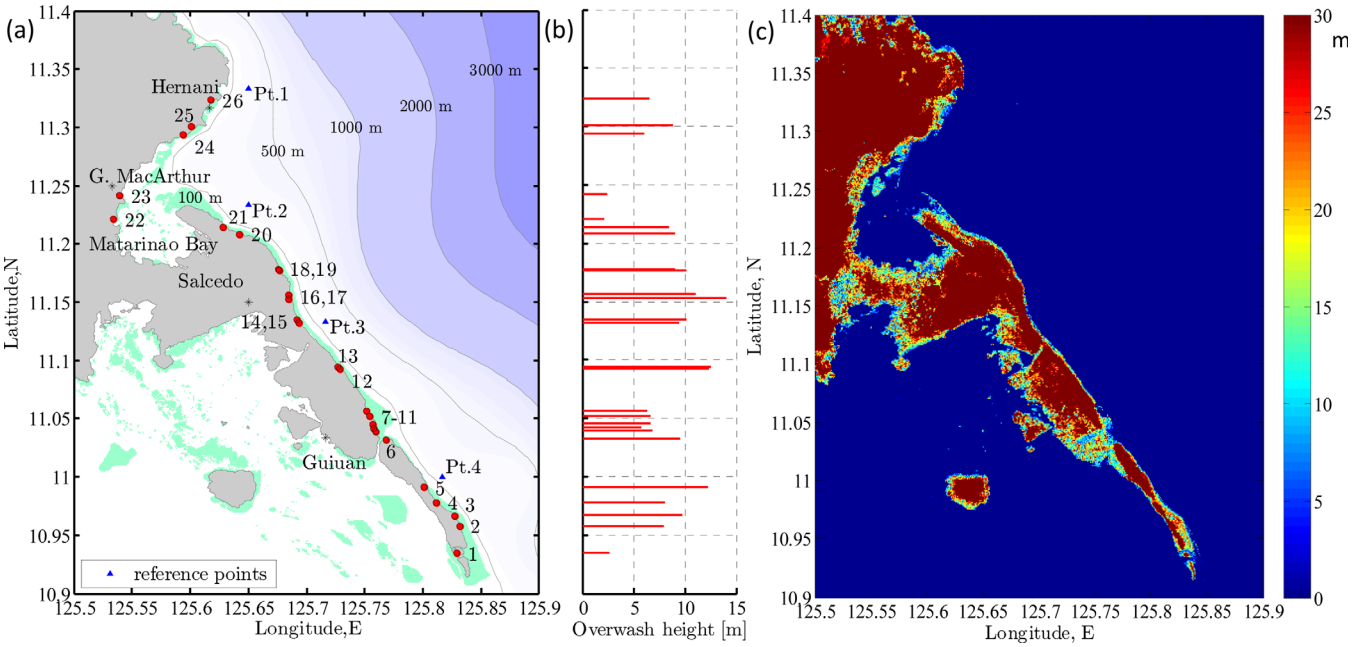

Figure 3. Distribution of storm overwash heights and bathymetry/topography of the study area. (a) Bathymetric map of the study area showing measured locations of the overwash heights and the coral reef distribution by green colored areas. (b) Measured overwash heights above mean sea level plotted against latitude. (c) Topographic map of the study area based on ASTER Global Digital Elevation Map.

and watermarks on trees and buildings (Figure 2d). Multiple types of evidence were often used to determine an overwash height at a site. Great care was taken to ensure that measured phenomena arose from water flows, since some evidence could also have resulted from strong winds. In the case that material evidence was not clear, we conducted local interviews to obtain reliable information of high water levels witnessed during or just after the event.

Elevation measurements were conducted once the measuring target was determined. Differential leveling was employed using an automatic level, taking the sea surface on the nearest shore as a datum. The horizontal positions of the target and the datum point were also recorded by a handheld GPS to obtain a horizontal distance from the shoreline. The datum of the elevation data was later transferred to the mean sea level considering the local tide level at the time of the measurement based on a global tide prediction model [*Matsumoto et al.*, 2000]. Finally, reliable data of the overwash height above mean sea level were obtained at a total of 22 sites.

2.2. Survey Results

Figure 3a shows the distribution of the survey sites with reliable overwash heights on a map of the survey area. The points numbered from south to north are irregularly distributed since accessible beaches are limited due to the hilly coastal topography. The figure also contains seafloor bathymetry (GEBCO data set) [*IOC et al.*, 2003] and coral reef distribution (Global distribution of coral reefs data set) [*UNEP-WCMC et al.*, 2010] around the survey area. The overwash heights at the 26 sites are plotted against latitude in Figure 3b, among which the four points (Pt. 9, 16, 17, and 25) were previously surveyed by *Tajima et al.* [2014]. More detailed information on the data set is provided in Table S1 of the supporting information. The adjacent reef width and the shore facing direction in the table were estimated from satellite images. Figure 3c shows a topographic map of the study area up to 30 m above the mean sea level based on ASTER GDEM by METI and NASA.

The survey results exhibit a large variation of overwash heights from 2.2 to 14.1 m. The variation is not monotonic and shows some significant drops in places along the coastline due to local topographic features. The small heights of 2.5–2.9 m were measured at sites sheltered from open ocean such as those inside Matarinao Bay. This supports that the storm surge was not the primary cause of the high water level since it should be rather amplified in a semienclosed shallow water basin. Overwash heights of similar magnitude were also observed throughout the western coast facing the Gulf of Leyte although they were not formally measured.

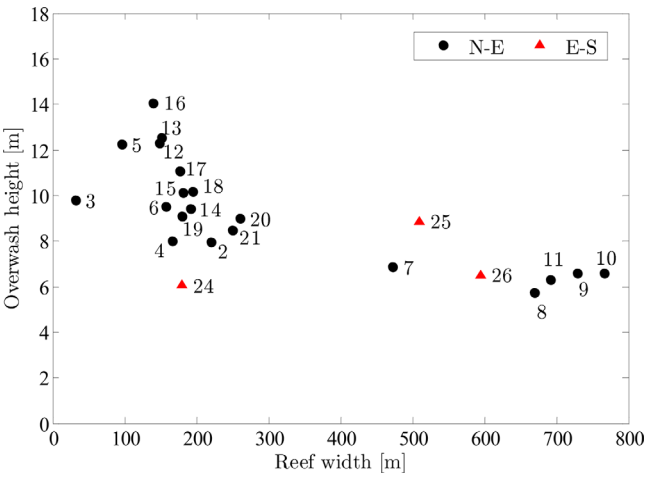

Figure 4. Relationship between overwash heights and adjacent reef widths classified by the shore facing direction.

Damages were relatively minor at these sheltered and western sites, and most dwellings adjacent to coastal swamps received minor inundation. In contrast, the overwash height was extremely large along the eastern coast directly exposed to the coastal storm. The maximum height of 14.1 m was recorded at Jagnaya (Pt. 16) in Salcedo where storm waves reached the roof level of a house standing on high ground behind a steep foreshore. Most of the overwash heights exceeding 10 m were found at sites with steep beaches and narrow reefs where high cliffs approach the shore (Figure 3c).

Another remarkable case, which characterizes this event, was found at Dumpao beach (Pt. 7–11) in Guiuan where a mild-slope sandy beach is fronted by a wide fringing reef. High watermarks at the site were found at relatively lower levels, about 6 m above mean sea elevation, while seawater intrusion reached about 1 km inland. This could not be caused by wind waves in the ordinary period range and strongly suggested the involvement of infragravity waves. The significance of the infragravity waves is also indicated by a case in Hernani (Pt. 26), a coastal village located in the northern part of the survey area. The small town on a coastal plain was severely devastated by repeated attacks of high waves. A video footage of a flooding wave was filmed by a witness at a house located about 80 m inland during the storm [*PLAN International Website*, 2014]. It shows that a large positive surge lasted for at least 20–30 s to wash away the house, indicating the overall wave period to be in the range of the infragravity waves.

Infragravity waves are known to be generated across the reef front through nonlinear wave interactions. The spectral component around the natural period of the reef flat, which is usually on the order of hundreds of seconds, can be significantly enhanced on the shore. The natural periods of the reef flat are given by the following equation if a basin of constant depth is assumed,

$$T_n = \frac{4W_r}{(2n+1)\sqrt{g(h_r+\bar{\eta})}}, \tag{1}$$

where T_n is the resonance period of the nth mode, W_r and h_r are the width and water depth of the reef flat, respectively, $\bar{\eta}$ is the wave setup, and g is the gravitational acceleration. The actual resonance period is slightly longer than given by equation (1) because of the reef friction to reduce wave celerity and the presence of the beach slope to extend the propagation distance. On the Eastern Samar coast, the reef water depth is about 0.5 m on average, while the reef width ranges from 30 to 800 m. Therefore, spectral wave characteristics may vary along the coastline according to the variation of the reef-flat resonance period. The resonance of the fundamental mode ($n = 0$) may be excited only in case of a small reef width even if a combination of the wave and wind setup of a few meters is taken into account. On the other hand, resonance of the higher-order modes could occur in a large portion of the coast without a significant rise in the mean water level.

Figure 4 shows the relationship between the measured overwash heights and the adjacent reef widths. The data points are classified into two types by the shore facing direction, northeast or southeast. The overwash height decreases with increasing reef width since more wave energy is lost through wave breaking and frictional dissipation. The relationship is very similar to those obtained in posttyphoon field surveys in Guam, although the overall magnitude is larger in Eastern Samar reflecting the strength of the typhoon [*Jaffe and Richmond*, 1993; *Ogg and Koslow*, 1978]. The overwash heights rapidly increase when the reef width becomes smaller than 200 m, which is also found in the result by *Jaffe and Richmond* [1993]. The similarity of the relationships despite different coastline geometries implies that the storm overwash on fringing reef coasts is strongly restricted by the adjacent reef width. It is, however, not clear how different spectral wave

components contribute to the relationship from this limited result. In order to look into further details, we develop a numerical model for wave transformation over fringing reefs to reproduce the field data.

3. Numerical Model

3.1. Model Description

Wave transformation over coral reefs has been long studied in the framework of the phase-averaged wave models. Many researchers have attempted to model wave attenuation due to wave breaking using the wave energy equation with a breaking model such as by *Battjes and Janssen* [1978] and to represent the resulting wave setup based on the concept of the radiation stress [*Gerritsen*, 1980; *Lowe et al*., 2005]. *Nakaza and Hino* [1991] conducted a representative study in this model framework to discuss the generation of infragravity waves. They confirmed through numerical tests that a low-frequency oscillation was resonantly excited due to temporal variations of radiation stress. *Massel and Gourlay* [2000] and *Sheremet et al*. [2011] employed an extended mild-slope equation model, while *Van Dongeren et al*. [2013] applied a wave-group model for the wave deformation over fringing reefs.

More recently, phase-resolving wave models have been developed to directly simulate the reef hydrodynamics in more detail. Most of them are based on the Boussinesq-type equations which are capable of describing nonlinear wave deformation of short period waves [*Skotner and Apelt*, 1999; *Nwogu and Demirbilek*, 2010; *Roeber and Cheung*, 2012]. In order to account for the effects of wave breaking, some incorporated an artificial dissipation term into the momentum equation based on turbulence models, while others employed the shock-capturing method to add nonlinear numerical dissipation. The model results suggested that the Boussinesq-type models can reproduce the nonlinear energy transfer to generate infragravity waves observed in laboratory experiments. Comparable performance has been achieved by a nonhydrostatic wave-flow model, SWASH [*Zijlema*, 2012; *Torres-Freyermuth et al*., 2012].

The present model is based on fully nonlinear weakly dispersive wave equations,

$$d_t+(du)_x=0, \tag{2}$$

$$d(\Gamma_0-\gamma d^2\Gamma_{0xx})=\left(\frac{d^3}{3}\Gamma_1-\frac{d^2}{2}\Gamma_2\right)_x+z_{bx}\left(\frac{d^2}{2}\Gamma_1-d\Gamma_2\right)-\frac{1}{2}f_w u|u|, \tag{3}$$

$$\Gamma_0=u_t+uu_x+g\eta_x, \tag{4}$$

$$\Gamma_1=u_{txx}+uu_{xx}-u_x^2, \tag{5}$$

$$\Gamma_2=z_{bx}(u_t+uu_x)+u^2z_{bxx}, \tag{6}$$

where t is time, x is horizontal coordinate, a subscript x or t denotes a derivative with respect to x or t, d is the total water depth, u is the depth-averaged horizontal velocity, η is water surface elevation, z_b is seabed elevation, f_w is the wave friction factor, and γ is a parameter to enhance the dispersion relationship of the model equation. The equations are identical to the fully nonlinear wave equations of *Seabra-Santos et al*. [1987] if γ is set to be zero, while they reduce to the enhanced Boussinesq equation of *Madsen et al*. [1991] if nonlinear terms with respect to u and η are neglected from the dispersion terms. Following *Madsen et al*. [1991], we choose $\gamma=1/15$ to minimize the discrepancy of the dispersion relation from that of the linear wave theory. The enhancement was done to extend the applicable range of the model equation to deeper water off the reef front. The bottom friction on the reef is represented by the quadratic law since existing laboratory and field studies are mostly based on the formulation, providing values of the friction factor f_w. The depth-averaged velocity is used instead of the nearbed velocity since the long wave approximation is likely to be valid on the shallow reef flat.

The effect of wave breaking is represented by applying the shock-capturing method to the governing equations. The method automatically detects discontinuities in solution and introduces nonlinear dissipation to suppress nonphysical oscillations arising from them. The validity of this approach for wave breaking over fringing reefs was confirmed in previous studies [*Roeber and Cheung*, 2012; *Zijlema*, 2012]. However, the shock-capturing methods are, in general, too diffusive when applied to short wave propagation and thus cannot accurately reproduce wave steepening to the breaking point. This may significantly affect mass and

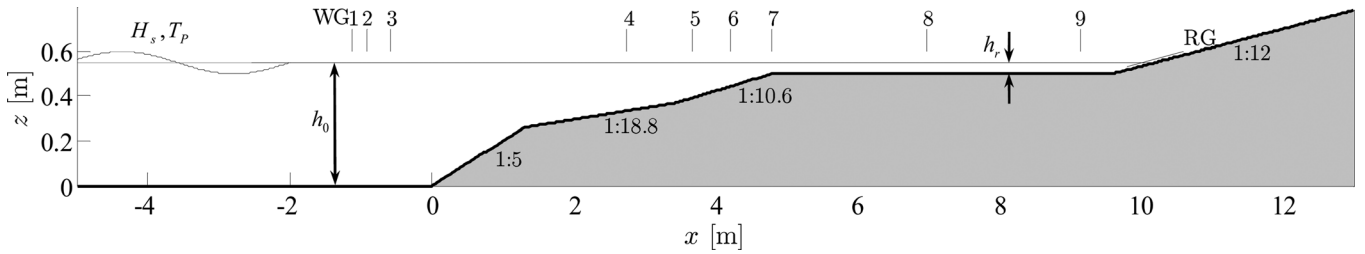

Figure 5. Bottom configuration and wave gage setup of the laboratory experiment by *Demirbilek et al*. [2007].

momentum transferred onto the reef flat. In order to simultaneously satisfy both requirements for low dissipation before breaking and rapid wave attenuation due to breaking, a higher-order finite difference scheme, which is called the base scheme hereafter, is hybridized with the shock-capturing method following *Yee et al*. [1999]. A switching function is used to make the dissipation active only in required parts of the computational domain. The characteristic-based dissipation associated with different shock-capturing methods such as TVD, ENO and WENO can be incorporated in the model. For more details regarding the numerical scheme, see Appendix A.

3.2. Model Validation

For validation of the present model, computed results are compared with measured data from laboratory experiments on wave deformation over fringing reefs by *Demirbilek et al*. [2007]. They carried out a series of well-instrumented experiments in a wind-wave flume with 35 m length, 0.7 m width, and 1.6 m depth as shown in Figure 5. A 1/64 scale fringing reef model was constructed at one end of the flume and irregular waves with different properties were generated from a plunger-type wavemaker at the other end. Water surface elevation was measured by wave gages at nine points, while shoreline inundation was recorded by a runup gage (RG) placed parallel to the sloping bed.

A total of 23 cases were selected for model validation from all 29 cases of the no-wind experiments with different incident wave heights, periods, and reef water depths as shown in Table S2 of the supporting information. The remaining cases were excluded owing to large values of the dispersion parameter, as the present model with weakly dispersive nature is not capable of simulating strongly dispersive waves. The experimental cases are divided into four groups by the reef water depth h_r, and several wave conditions are considered in each group. For creating incident irregular waves in the experiments, JONSWAP spectra with a peak enhancement factor of 3.3 were employed with various peak periods T_p and significant wave heights H_s.

Numerical simulations were carried out for the 23 cases with a spatial resolution of $\Delta x = 3$ cm. The incident boundary was placed at the location of wave gage 1 and incident wave profiles of 15 min duration were created from the measured data with a time step of $\Delta t = 0.0025$ s. In order for outgoing waves to transmit out from the computational domain, the Sommerfeld's radiation condition with the sponge layer technique was applied to the reflected wave component at the incident boundary [*Ohyama and Nadaoka*, 1991]. The wetting-drying treatment for simulating shoreline movements was based on the thin-water-layer approach, in which a thin water film of $h_d = 0.1$ mm is maintained in dry zones. The wave friction factor f_w was set to be a small value of 0.005 as the reef model was made of polyvinyl chloride plastic with a smooth surface. The switching function for the characteristic-based dissipation was defined as the logistic function of the spatial coordinate x,

$$\theta(x) = \frac{1}{1 + e^{-\kappa \frac{x - x_{sw}}{L_{sw}}}}, \tag{7}$$

where x_{sw} is the switching position given by the equation $h(x_{sw}) = H_s$, L_{sw} is the local wavelength at the position and κ is the constant to determine the transitional length. The same switching function was employed for both components of $m = 1$ and 2 in equation (A9). Therefore, the characteristic-based dissipation is incorporated only where the water depth is smaller than the incident wave height. The parameter κ is set to be 20 so that the value of the function transitions from 0 to 1 approximately over a half local wavelength.

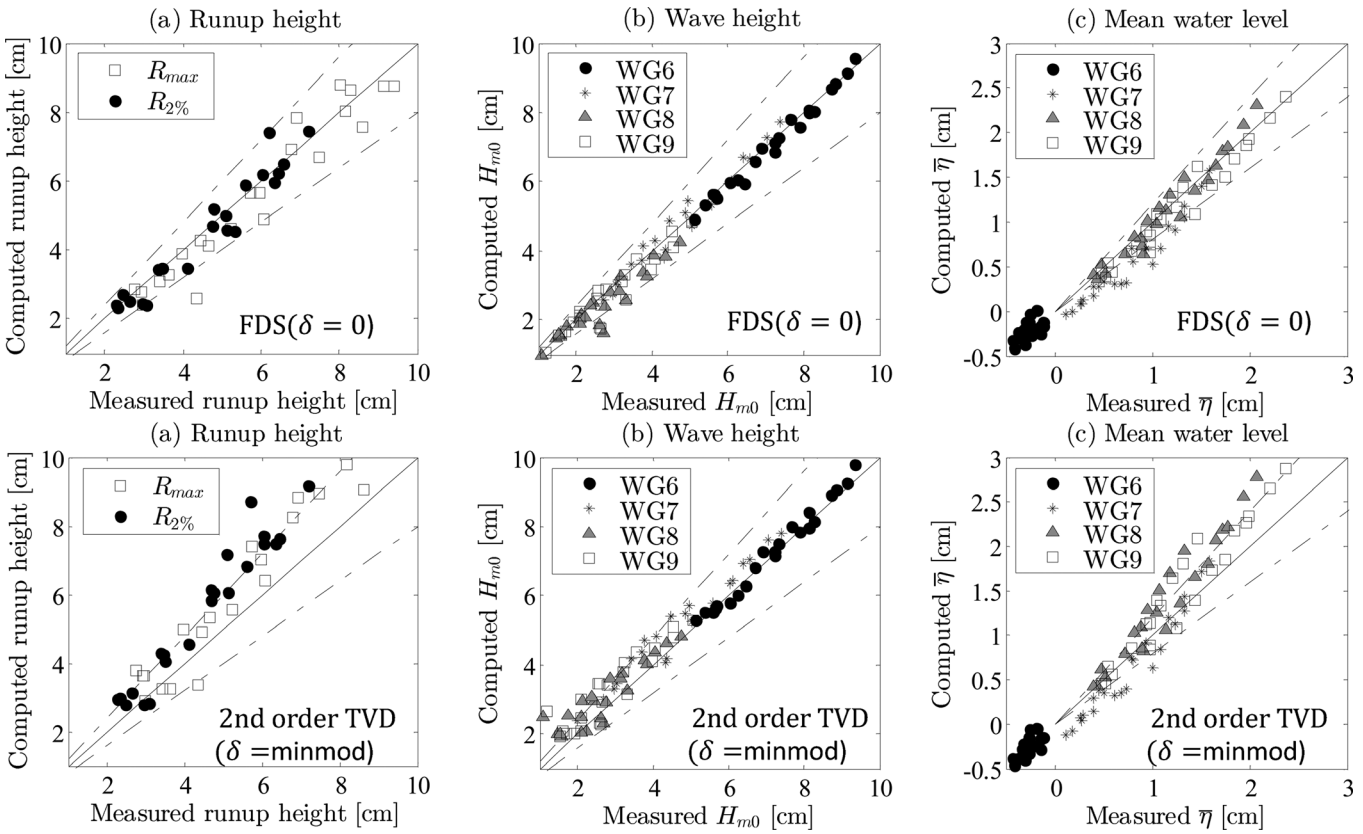

Figure 6. Measured and computed runup height, R_{max} and $R_{2\%}$, significant wave height H_{m0} and mean sea level $\bar{\eta}$ by the (top) FDS-based and (bottom) TVD-based dissipation model. The broken lines indicate a relative difference of ±20%.

Therefore, incoming waves going beyond the breaking limit exhibit nonphysical oscillations over the reef front, which are suppressed by the dissipation to represent wave decay due to wave breaking. The characteristic-based filters associated with two different schemes are employed here: the second-order TVD scheme with the minmod limiter and Roe's flux difference splitting (FDS) scheme. The former is a high-resolution method that is widely used to capture discontinuous profiles sharply in hydrodynamic problems such as bores and hydraulic jumps. The latter is highly dissipative, providing more numerical dissipation than is required to suppress numerical oscillations.

Computed runup heights, significant wave heights, and mean water levels at different locations are compared with measured data for all of the 23 cases in Figure 6. The top and bottom plots show results by the FDS-based and the TVD-based filters, respectively. The maximum runup height, R_{max}, and highest 2% runup height, $R_{2\%}$, are simulated better in the top figure than in the bottom figure with a few exceptions. The systematic overestimation of the TVD-based filter is also confirmed in the comparison of significant wave heights in the middle plot. Significant wave heights at WG6 in front of the reef edge are reproduced well in both results, but computed results at WG8 and WG9 on the reef flat are consistently larger than measured values using the TVD-based filter. These comparisons suggest that rapid wave decay on the reef front due to wave breaking is not fully accounted for by the TVD-based dissipation which just preserves monotonicity of the solution. Therefore, the FDS-based filter with further dissipation is more successful in simulating wave energy on the reef flat. Consequently, the wave setup on the reef flat is overestimated as well in the bottom plot, since the shoreward radiation stress acts on shallower water due to the prolonged wave attenuation. It is worth noting that linearizing the dispersion terms of the model equation leads to overestimation of waves entering the reef flat due to the absence of antisteepening effects.

In order to compare the model performance among experimental conditions, cross-shore profiles of the significant wave height and the mean water level are plotted for six representative cases in Figure 7. The numerical results based on two different dissipation models are graphed with measured data in each plot.

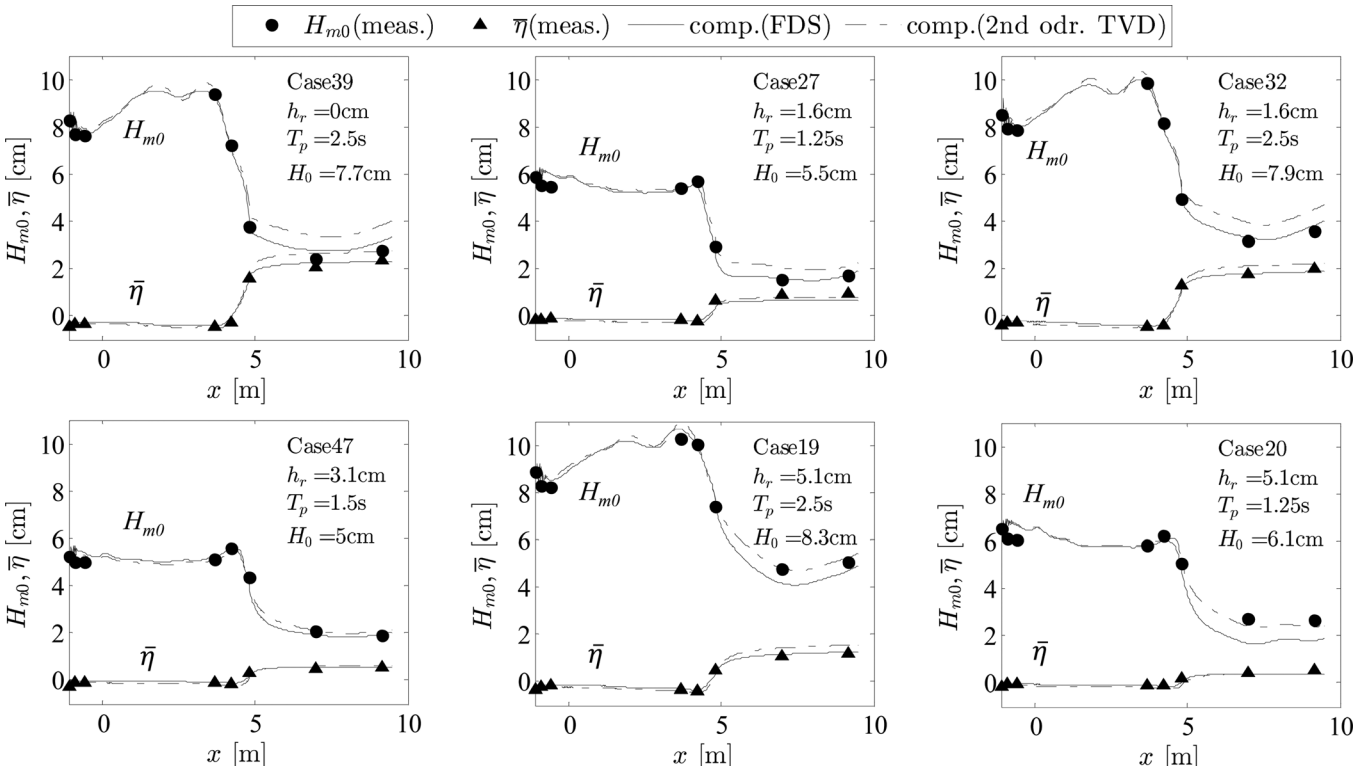

Figure 7. Measured and computed distributions of significant wave height H_{m0} and mean sea level $\bar{\eta}$ over the reef flat for six representative cases.

The computed profiles of significant wave heights by the two models agree well with the measured profiles up to WG7 in all the cases. The FDS-based filter gives better results for wave transformation across the reef front in cases of the shallower reef flats ($h_r = 0$ cm and 1.6 cm), whereas the TVD-based filter performs better in case of the deeper reef flat ($h_r = 5.1$ cm). Measured and computed surface elevations for three representative cases (Case 39, 32, and 19) at different cross-shore locations are compared in time and frequency domains in Figure S1 of the supporting information. Both models successfully reproduce the energy transfer to the lower-frequency band. The TVD-based filter tends to overestimate the low-frequency component, while the FDS-based filter underestimates the high-frequency component, which leads to the discrepancy of the two model results in Figure 7. Since we are at present focusing on the problem with shallow fringing reefs, the following discussion will be made with the FDS-based filter. It should be, therefore, noted that the model may lead to the underestimation of high-frequency components although they are subject to strong frictional dissipation on the rough surface of actual reefs.

4. Field Application

To elucidate the underlying mechanism of the observed wave impacts, we investigate extreme wave characteristics on the Eastern Samar coast through model applications. Offshore wave conditions and local water depth on the reef flat during the passage of the typhoon are estimated by a wave hindcast and a storm surge simulation using a parametric typhoon model. Under the estimated boundary conditions, wave evolution over one-dimensional reef topographies is simulated with varying reef widths and beach slopes. To overcome uncertainties in model input parameters, we perform a parametric analysis and validate the model results against the overwash heights from the field surveys. Finally, we discuss spectral and temporal characteristics of wave runup on the coast using the optimized model results.

4.1. Model Boundary Conditions

Incident wave properties off the fringing reef are essential to model wave propagation and inundation on the coast. Without wave observation data, we estimate the deep water wave conditions using the third-generation

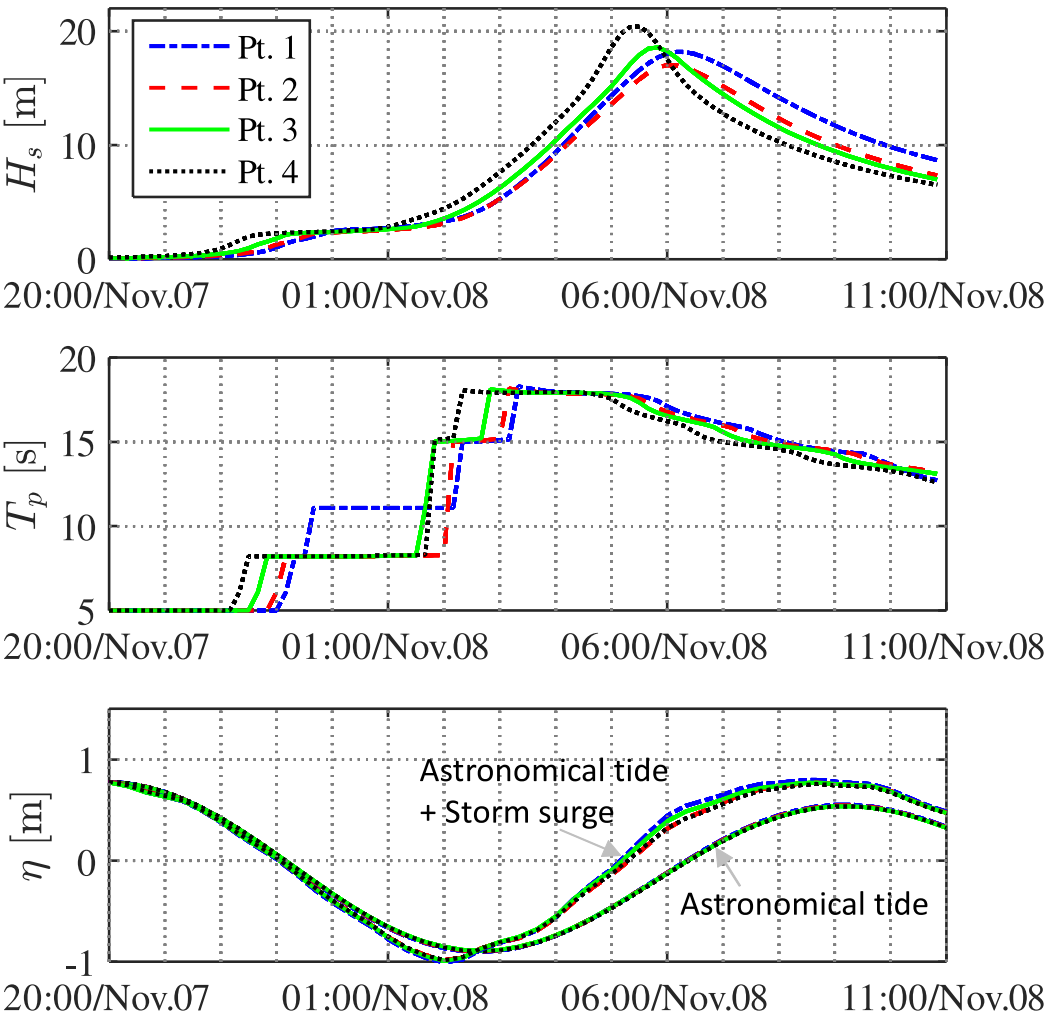

Figure 8. Results of wave hindcast, astronomical tide, and storm surge model at the four reference points. (a) Significant wave height H_{m0}. (b) Peak wave period T_p. (c) Local tide level with and without sea level anomaly due to storm surge.

wave hindcasting model, WAM [*The Wamdi Group*, 1988]. Computational grids based on spherical coordinates are created with a spatial resolution of 2 min latitude/longitude to cover the track of the typhoon approaching the Eastern Samar coast as shown in Figure S2 of the supporting information. The pressure field by the typhoon is produced by the formula of *Myers* [1954] with the central pressure from the best track data. The radius of the maximum wind speed was also estimated from the central pressure using an empirical relation based on data from 842 historical typhoons [*Kato*, 2005]. The rotational gradient wind field is calculated from the pressure field considering the super gradient feature in the eye-wall region [*Mitsuta and Fujii*, 1987] and then combined with translational wind speeds to make wind input data. The air-sea drag coefficient is evaluated by the formula of *Oey et al.* [2006], which considers its reduction for high wind speeds in tropical cyclones. The energy balance equation with source terms of wind input, nonlinear transfer, and wave energy dissipation, is numerically integrated with a time step of 10 s. A two-dimensional spectrum with 36 directions and 24 frequencies is output at an interval of 10 min for a total time of 30 h. The computed spatial distribution of the maximum significant wave height is shown in Figure S2 of the supporting information.

Figures 8a and 8b show temporal variation of significant wave height H_s and peak wave period T_p at four points off the southeastern coast of Eastern Samar. The reference points are laid out along the 100–200 m depth contour line as indicated in Figure 3a. The significant wave height is calculated as four times the square root of the zeroth moment of the computed wave spectrum, while the peak wave period is obtained

as the maximum of a parabolic fit to the three bins around the spectral peak. The wave height started growing around 22:00 on 7 November and came to a peak around 6:00 on 8 November (local time). According to local interviews on the coast, the seawater inundation started around 5:00 on 8 November, which matches with the time of rapidly growing wave height. The peak value of the significant wave height ranges from 16 to 20 m, gradually increasing to the south. The peak wave period at that time takes a nearly constant value of 16.5 s regardless of the location. Although the computed values should be regarded as a rough estimate due to uncertainties in wind profiles, they suggest that huge waves with significant height of over 15 m propagated to the reef front during the peak time.

Besides the wave generation, the mean water level was also raised due to low-pressure suction and wind setup by the typhoon. Although the sea level anomaly is expected to be small due to the steep offshore topography, the reef flat is originally so shallow that its relative contribution to the local water depth is not negligible. In order to estimate the reef water depth in the passage of the typhoon, we perform a storm surge simulation in a larger domain with a finer resolution of 30 s longitude/latitude, using the same wind data created for the wave hindcast. The storm surge model is based on the 2-D nonlinear shallow water equations with the pressure and wind stress terms. The effect of wave setup is not accounted for and will be discussed separately with the present wave model. The astronomical tide level during the period was separately calculated using the global tide model, Naotide [*Matsumoto et al*., 2000]. The computational domain and the distribution of the maximum sea level anomaly are shown in Figure S3 of the supporting information.

Figure 8c shows temporal variation of water surface elevation with and without the storm surge in the passage of the typhoon. There is no significant difference in both astronomical tide levels and storm surge heights at different locations. The local water surface started rising around 3:00 on 8 November and reached the maximum elevation of 0.7 m above mean sea level around 8:00 on the same day. At the peak time of the significant wave height, the astronomical tide level was slightly lower than the mean sea level, while the sea level anomaly due to the storm surge was about 0.6 m. Assuming the mean reef water depth to be 0.5 m, the reef-flat water depth at the peak time is, therefore, estimated to be about 1.0 m excluding the contribution of the wave setup. The computational grid of 30 s latitude/longitude does not resolve the reef bathymetry and thus the actual wind setup could be higher due to the shallower water. However, the local setup is estimated to be small because the wind fetch of several hundreds of meters is not sufficient to develop a significant surge.

4.2. Model Sensitivity Analysis

Using the proposed wave model, we investigate wave characteristics over the fringing reefs on the Eastern Samar coast during the highest stage of offshore wave development. Fundamental wave characteristics can be derived by the 1-D model by disregarding two-dimensional wave deformation. It should be, however, noted that progressive and standing edge waves could be generated over fringing reefs even for a straight coast [*Cheung et al*., 2013; *Roeber et al*., 2010], and therefore this aspect should be taken into account with 2-D models to capture full details of the actual phenomena. The model topography is simplified to a combination of the reef flat of length W_r and depth h_r and two uniform slopes $\tan\beta_r$ off the reef and $\tan\beta$ on the shore as illustrated in Figure 9. The reef width and beach slope vary significantly along the coastline, whereas the fore-reef slope seems to be uniform and thus assumed to be $\tan\beta_r = 1/10$ from the local bathymetric chart. The water depth h_r on the reef flat during the highest stage of wave development was previously estimated to be 1.0 m. The incident wave boundary is placed at a depth of $h_0 = 80$ m and approximately 1.2 km offshore of the reef edge in such a way that the resulting dispersion parameter for the peak wave period falls within the previously validated range.

We first perform a sensitivity analysis to clarify the influences of uncertain physical parameters on the extreme reef hydrodynamics. Numerical simulations are conducted with different model parameters by resolving the model bathymetry at $\Delta x = 3$ m resolution. The incident wave spectrum was created by fitting a JONSWAP spectrum to the computed spectrum averaged over 1 h around the peak time (6:00 on 8 November) and the four reference locations in Figure 8. The selected peak time agrees with the time of the maximum inundation from local interviews. The resulting significant wave height and peak wave period were $H_s = 17.3$ m and $T_p = 16.5$ s, respectively. The peak enhancement factor was estimated as 1.5 by a technique of *LeBlond et al*. [1982] (see Figure S4 of the supporting information for the computed and fitted

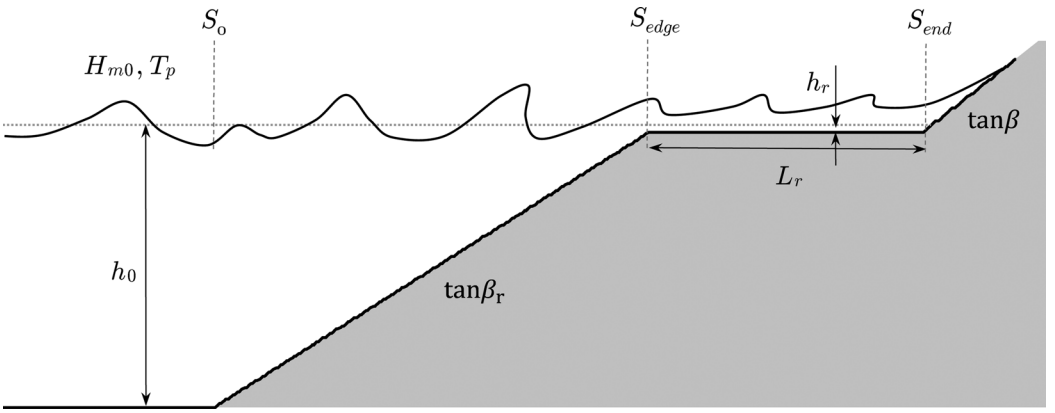

Figure 9. Model bathymetry for wave simulations on the Eastern Samar coast and definitions of the geometric parameters.

wave spectra). Although the incident wave spectrum was obtained in deeper water, we directly give it at the model incident boundary (h_0=80 m) as the shoaling effect in the relatively deep water is likely to be smaller than the uncertainty in the wave hindcast. The duration of each model run is set as 3 h to obtain a large number of individual waves for following statistical and spectral analyses. Two different friction factors on the reef and the remaining areas are defined as f_w and f_{w0}, respectively. The former is treated as an unknown model parameter, while the latter is fixed at 0.01. For the characteristic-based dissipation, the FDS-based filter is employed here, which performs better on shallow fringing reefs and also brings higher stability for the long lasting computation of drastic wave deformation.

To calibrate the model parameters with the field data, we estimate the maximum runup height on the coast from the model results. Large-scale experimental investigations by *Grüne* [2005] have confirmed that a natural debris level after a storm event corresponds to the maximum runup height during the storm. Since majority of the overwash heights from the field surveys were based on the most landward debris lines, the maximum runup height from the model should lie in the same level. We first obtain the shoreline elevation $R(t)$ as modeled water surface elevation at the most landward wet cell and then individual runup heights $\hat{R}$ by the crest method following *Mase and Iwagaki* [1984] (see Figure S5 of the supporting information for a schematic). Since the numerical time series of shoreline elevation is not always smooth, the local maxima with widths greater than 3 s are only counted. The frequency analysis of the individual runup heights $\hat{R}$ suggests that they follow the Weibull distribution (see Figure 15 for runup histograms):

$$P_r(\hat{R}) = \frac{c}{b}\left(\frac{\hat{R}}{b}\right)^{c-1} \mathrm{e}^{-(\hat{R}/b)^c}, \tag{8}$$

where $P_r(\hat{R})$ is the probability of the runup height being equal to $\hat{R}$, b is the scale parameter and c is the shape parameter of the distribution. From this follows that the probability density function of the maximum value $\hat{R}_{max}$ of the individual runup heights in a sample of size N may be written as

$$P_r(\hat{R}_{\max}) = N\frac{c}{b}\left(\frac{\hat{R}_{\max}}{b}\right)^{c-1}\left\{1-\ \mathrm{e}^{-(\hat{R}_{\max}/b)^c}\right\}^{N-1} \mathrm{e}^{-(\hat{R}_{\max}/b)^c}, \tag{9}$$

where $P_r(\hat{R}_{\max})$ denotes the probability that any one of N runup heights shall not exceed $\hat{R}_{\max}$. We define the maximum runup height R_{max} as the most probable value of $\hat{R}_{\max}$ corresponding to the peak of the probabilistic density function given by equation (9). The parameters b and c are estimated by the most likelihood method based on the sample of 3 h duration, while N is determined as a number of runup waves in 1 h duration for which the incident wave spectrum was created. The resulting R_{max} provides a statistically robust estimate of the maximum runup height during the intensive storm period on the coast.

To validate the model incident wave, we compute the maximum runup heights with different values of H_s around the hindcast value of 17.3 m. Figure 10a shows the relationships between the maximum runup

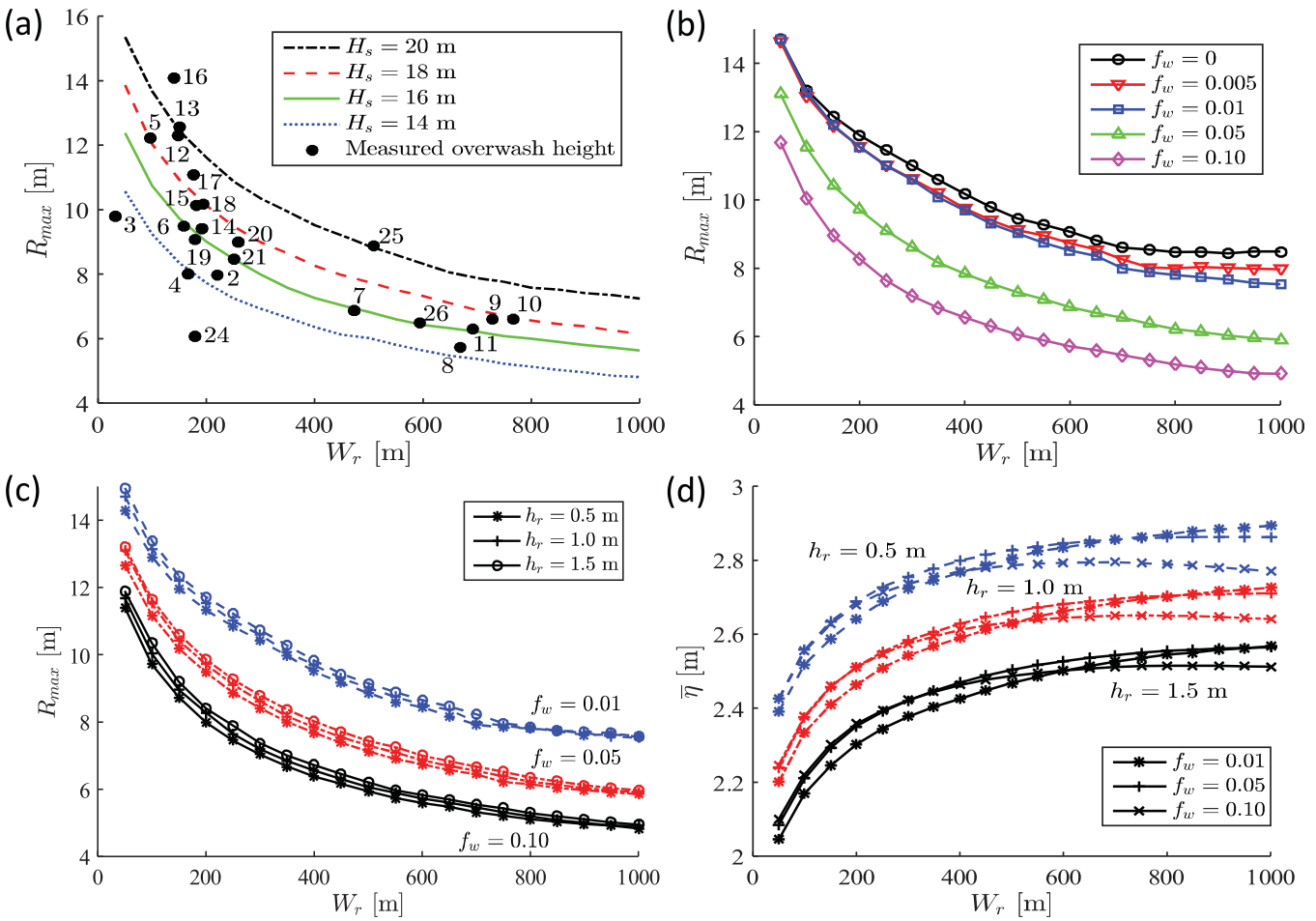

Figure 10. Results of the model sensitivity analysis with varying reef width. (a) R_{max} by different incident wave heights. (b) R_{max} by different friction factors. (c) R_{max} by different friction factors and reef water depths. (d) $\bar{\eta}$ by different friction factors and reef water depths.

height R_{max} and the reef width W_r under incident wave heights of H_s=14, 16, 18, and 20 m and the distribution of the measured overwash heights. The other parameters are set as follows: f_w=0.04, h_r=1.0 m, and tan β=1/10. The maximum runup height decreases with increasing reef width. The curves have a similar form and shift vertically in proportion to the incident wave height. Comparing the model and field data confirms that H_s = 17.3 m is a reasonable estimate, provided that the other parameters are in a valid range. With a larger (smaller) incident wave height, an unreasonably high (low) friction factor is required to fill the discrepancy in the two results as we demonstrate later. The following analyses will be based on the hindcast value of H_s=17.3 m unless otherwise noted.

Figure 10b shows the maximum runup curves resulting from five different values of the friction factor (f_w = 0, 0.005, 0.01, 0.05, and 0.10). The initial reef water depth and the beach slope were fixed at h_r=1.0 m and tan β=1/10, respectively. The frictional effect on the reef surface significantly reduces the runup height when f_w is greater than 0.01. The friction on the fore-reef slope reduces incoming waves to the reef flat, while the reef-flat friction dissipates the postbreaking waves more significantly on a wider reef. The no-friction result suggests that the rapid decrease of the runup height in the range of the small reef width (W_r < 500 m) is primarily attributed to prolonged wave-breaking dissipation that lasts until stable wave heights compatible with reef water depths are attained. The reef-flat resonance may also contribute to enhance the runup height in the range of small reef widths.

The influence of the reef water depth on the maximum runup height is presented in Figure 10c. The reef water depth takes three different values around the estimated value h_r = 0.5, 1.0, and 1.5 m considering the

uncertainty in the estimation. The larger water depth results in a higher runup, but the difference is small within the range of the reef water depth. The relationships between the wave setup averaged over the reef flat and the reef width are graphed for the same cases in Figure 10d. The radiation stress by the furious wave breaking at the reef front and the prolonged wave dissipation on the reef flat yields a wave setup of 2.5–2.9 m. The setup increases with the reef width to a certain limit, after which it stays at a almost constant value. The shallower reef flat leads to a larger wave setup as the steeper slope of water surface is required to balance with the shoreward radiation stress. The friction factor affects the wave setup in a complex manner as the frictional effects of the fore-reef slope and the reef flat differently influence the net force balance of the reef water. Consequently, the mean water depth on the reef flat ranges from 3.4 to 4.0 m depending on the reef water depth and the friction factor.

Given the hindcast wave height of H_s=17.3 m, the model output agrees with the field data when the friction factor is set to be about 0.04. However, different combinations of the incident wave height and friction factor could produce runup curves that fit well with the field data. To validate the present combination, we estimate the friction factor independently of the field data using an existing friction formula in the rough turbulent regime. *Swart* [1974] gives an explicit approximation of the semiempirical formula by *Jonsson* [1966] as

$$f_w = \exp\left\{5.213\left(\frac{A_b}{k_s}\right)^{-0.194} - 5.977\right\}, \tag{10}$$

where A_b is the wave excursion amplitude at bottom and k_s is the Nikuradse roughness parameter. *Madsen* [1994] introduced the representative bottom velocity amplitude u_{bm} and angular frequency ω_m to apply the same type of the friction formula to irregular waves,

$$A_b = \frac{u_{bm}}{\omega_m}, \tag{11}$$

and

$$u_{bm} = \sqrt{2\int S_{u_b} d\omega}, \quad \omega_m = \frac{\int \omega S_{u_b} d\omega}{\int S_{u_b} d\omega}, \tag{12}$$

where S_{u_b} is the spectrum of the bottom velocity, which can be obtained from the wave spectrum using the linear wave theory. Therefore, the friction factor can be estimated from the model results and compared with the presumed value for validation.

Figure 11a shows the variation of the representative bottom velocity amplitude u_{bm} and angular frequency ω_m at the middle point of the reef flat resulting from the parameter set: H_s=17.3 m, f_w=0.04, h_r=1.0 m, and tan β=1/10. The velocity amplitude decreases with increasing reef width due to energy dissipation by wave breaking and reef friction. The angular frequency shows a similar decreasing trend mainly due to the loss of short wavelength components. The wave excursion amplitude A_b remains constant for narrow reef widths, but increases in the range of large reef widths (Figure 11b). The resulting friction factor from equation (10) shows only a slight decrease over a wide range of the reef width as shown in Figure 11c. Hence, the use of a constant friction factor over different reef widths may be a good assumption in the present case. The three results based on different roughness parameters k_s suggest that k_s= 0.5–1.0 m is required to have f_w=0.04, which is much larger than the physical roughness of the reef surface observed in the field. *Lowe et al.* [2005] proposed the following relation between the roughness parameter and the roughness amplitude σ_r of the reef surface,

$$k_s = 4\sigma_r. \tag{13}$$

Although it is based on a limited number of wave dissipation measurements in the field, the relation gives the roughness amplitude of 13–25 cm for f_w=0.04. The actual roughness amplitude was in the similar range from visual observation in the field (Figure 2c). Therefore, the presumed value of f_w=0.04 falls in the reasonable range from the view of boundary layer flow characteristics. Past field studies presented the friction factor of $O(10^{-1})$ on the fringing and barrier reefs based on wave dissipation measurement [*Gerritsen*, 1980;

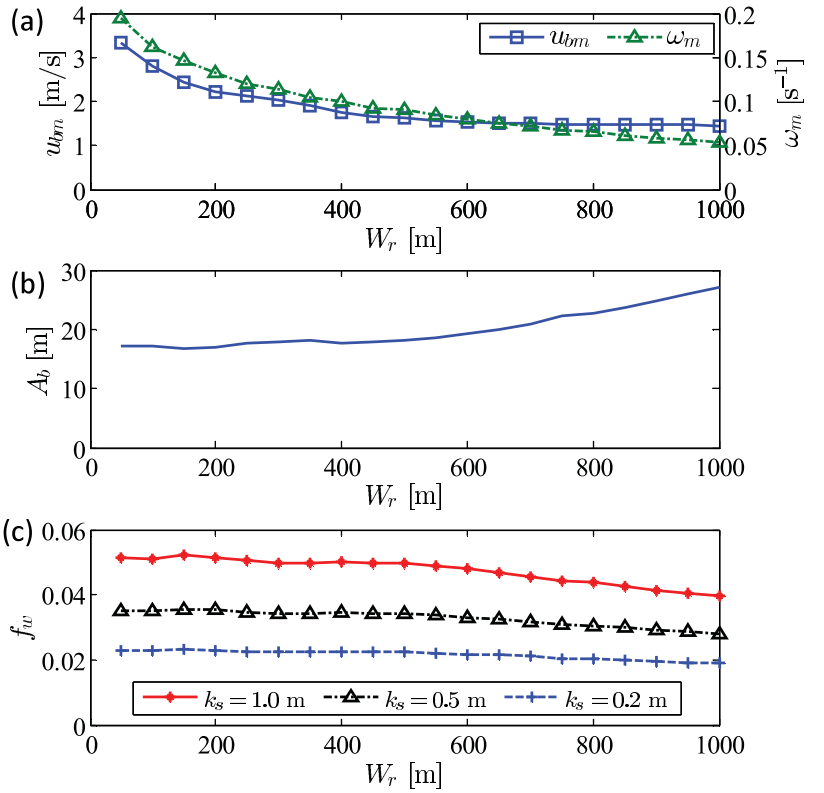

Figure 11. Estimation of the friction factor on the reef surface. (a) Representative bottom velocity amplitude u_{bm} and angular frequency ω_m. (b) Wave excursion amplitude on the bottom A_b. (c) Estimated friction factors f_w for k_s=0.2, 0.5, and 1.0 m.

Nelson, 1996; *Falter et al*., 2004; *Lowe et al*., 2005]. The main reason for the discrepancy is that the wave excursion amplitude is large relative to the reef roughness under extreme conditions, whereas the past studies were mostly conducted under normal wave conditions. Figure S6 of the supporting information presents A_b and f_w resulting from different incident wave heights (H_s= 14, 16, 18, and 20 m). The results suggest that f_w does not significantly change with the incident wave height. This puts a bound on the choice of f_w to ensure that the present combination of H_s and f_w is in a valid range.

The last parameter to be examined is the beach slope tan β, which is also a crucial parameter affecting the maximum runup height. On the Eastern Samar coast, the beach slope varies along the coastline due to the presence of limestone hills and other local landforms and thus cannot be represented by a single value. Here we consider four slopes tan β=1/5, 1/10, 1/20, and 1/30 covering its typical range. In order to see the effects of the beach slope, maximum runup curves with different slopes are plotted in Figure 12. For comparison purposes, the measured overwash heights are plotted together in the same figure. The beach slope greatly contributes to the maximum runup height especially in the range of small reef widths. The data points of the overwash heights, though they are highly scattered due to many other factors such as two-dimensional wave deformation, lie around the four runup curves. The actual beach topography consists of a steep foreshore slope and a milder backshore slope or a horizontal plane and thus we need to consider actual topographic features for further precise discussion. In the present model framework with the simplified topography, the determined parameter set best describes the field results.

4.3. Wave Characteristics

4.3.1. Wave Deformation Over Fringing Reefs

We discuss wave characteristics over fringing reefs on the basis of the model results previously obtained. Spectral wave properties are first explored to see how different spectral components contribute to the extreme flood on the coast. Figure 13a shows wave spectra off the reef S_0, at the reef edge S_{edge}, at the landward end S_{end} and of the shoreline elevation S_R for six cases with different reef widths and beach slopes

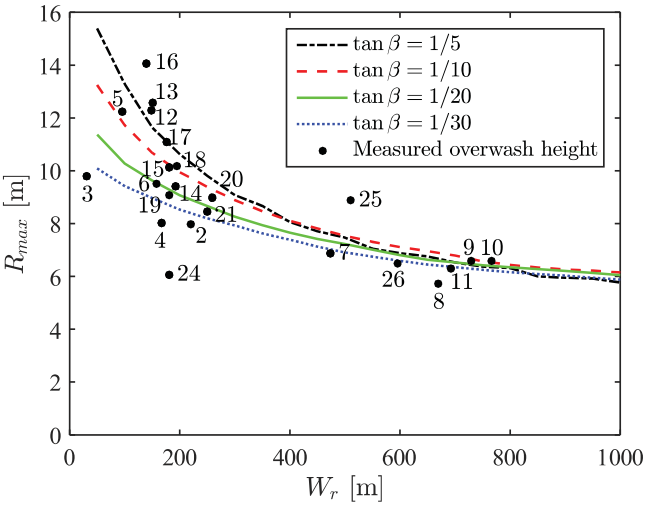

Figure 12. Relationships between the maximum runup height and the reef width for different beach slopes.

(see Figure 9 for their locations). The power spectrum is estimated from the computed time series of about 3 h by Welch's method with a Hanning window [*Welch*, 1967]. The reef width is different in top three plots (Cases 1, 2, and 3 with $W_r = 200$, 400, and 800 m) with the beach slope fixed at 1/10, while the beach slope is different in following two plots (Cases 4 and 5 with $\tan\beta = 1/5$ and 1/20) with the reef width fixed at 400 m. The last plot shows the results by the same reef width and beach slope as in Case 2, but with the reef friction off (Case 6).

The differences between S_0 and S_{edge} suggest that a large portion of incident wave energy around its peak frequency is dissipated by wave breaking at the reef front, while other portion is shifted to a lower-frequency band through the nonlinear energy transfer [*Symonds et al*., 1982; *Pomeroy et al*., 2012]. The spectrum at the reef edge does not vary with the reef width except that V-shaped depressions indicating creation of nodes due to the reef-flat resonance appear at different frequencies. Although corresponding antinodes are not obviously visible on the spectra at the reef end, the periods of the depressions agree with the reef-flat resonance periods from equation (1), which are indicated by dotted vertical lines in each plot. This is seen more clearly by plotting the spectral ratio S_{end}/S_{edge} in Figure 13b. There are distinctive peaks around the resonance frequency of the fundamental mode and much weaker ones around the higher-order resonance frequencies. However, a comparison of Cases 2 and 6, of which difference is none other than the friction factor, reveals that the node-antinode structure is largely suppressed by the reef friction.

The spectral change from S_{end} to S_R suggests the presence of another resonance phenomenon on the sloping beach shoreward of the reef flat. The spectral ratio S_R/S_{end} in Figure 13c exhibits a large peak at a certain frequency that varies not with the reef width, but with the beach slope. The spectrum at the reef end S_{end} creates a node at the frequency in the left plots. The runup spectrum S_R is enhanced on its lower-frequency side, while it is suppressed by wave breaking on its higher-frequency side. Comparing Cases 2, 4, and 5 with the same reef width, but with different beach slopes reveals that the runup amplification occurs in a lower-frequency band on a milder beach slope. This amplification is known to be caused by resonant wave interactions over plane beaches. *Stefanakis et al*. [2011], in the framework of the nonlinear shallow water equation, suggested that the runup of monochromatic waves is highest when the wave period satisfies the following relation,

$$T_R \approx \frac{5.1l}{\sqrt{gl\tan\beta}}, \tag{14}$$

where T_R is the runup resonance period and l is the beach length that is currently expressed by $l=(h_r+\bar{\eta})/\tan\beta$. The calculated value of T_R in each case is indicated in Figure 13c to show that the peak occurs at the period given by equation (14). It seems that the runup amplification is influential on flood characteristics as it occurs in the central band of the wave spectrum.

The two resonance phenomena, reef-flat resonances, and resonant runup amplification are combined in reef hydrodynamics under extreme conditions with a significant runup on the shore. Here the shoreline does not behave as in the case of a vertical wall at the reef end, and the shoreline motion is enhanced at a certain period depending on the beach slope. Therefore, the two resonances influence one another just like a coupled oscillator. The runup resonance affects the reef-flat resonance especially under the condition that the two resonance periods are close. Equating equations (1) and (14) suggests that the situation takes place when the following relation is satisfied,

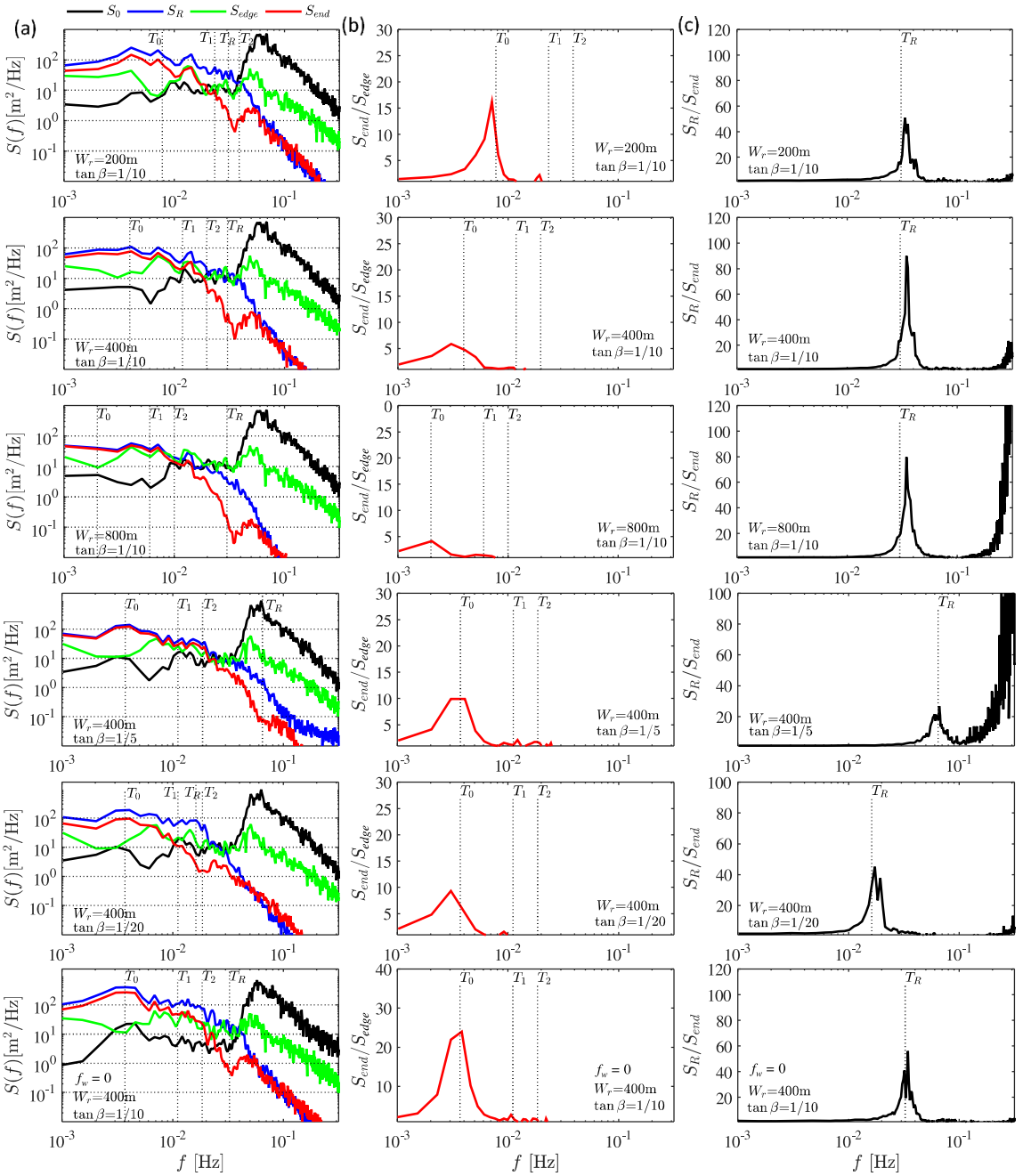

Figure 13. Changes in wave spectra over fringing reefs for six different cases. (a) Wave spectra offshore of the reef front S_0, at the reef edge S_{edge}, at the reef end S_{end}, and of the shoreline elevation S_R. (b) Ratio of S_{end} to S_{edge}. (c) Ratio of S_R to S_{end}.

$$\frac{W_r \tan\beta}{(h_r+\bar{\eta})} \approx 1.3(2n+1). \tag{15}$$

Within the present range of the parameters, the resonance periods T_1 and T_2 are close to T_R except for the cases with large reef widths or steep beach slopes. This probably explains why the higher-order resonances on the reef flat are not clearly observed even for the case of no reef friction in Figure 13.

To investigate the spectral wave characteristics comprehensively over different cases, we obtain significant wave heights of different spectral bands from S_{end} and S_R. The wave data are divided into three components according to the definition by *Munk* [1950]: very low frequency (VLF, $T \geq 300$ s), infragravity (IG, 30 s $\leq T <$

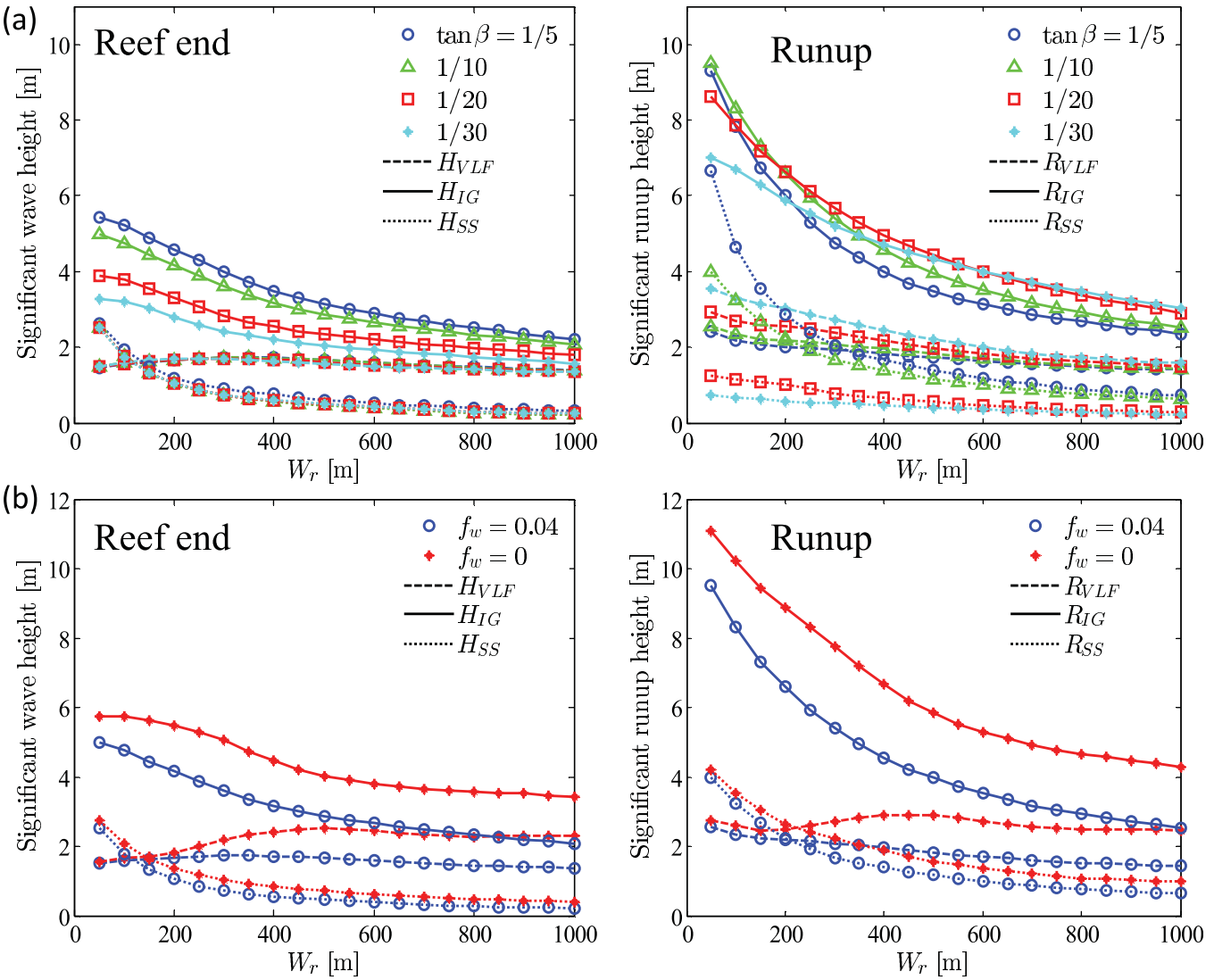

Figure 14. Relationships between significant wave (runup) heights of different spectral components and the reef width ((left) reef end and (right) runup). (a) Different beach slopes (f_w=0.04). (b) Different friction factors (tan β=1/10).

300 s), and sea-swell components (SS, $T < 30$ s). The significant wave heights H_{VLF}, H_{IG}, and H_{SS} (R_{VLF}, R_{IG}, and R_{SS} for the shoreline elevation) are calculated as four times the square root of the zeroth-order moment of the wave spectrum in each band and plotted against the reef width for different beach slopes in Figure 14a.

In the left plot showing the significant wave heights at the reef end, the IG component, which dominates the other two, shows a declining curve as the reef flat becomes wider. The contribution of the reef-flat resonance is not clearly confirmed, but it certainly increases the IG component in the range of the small reef width ($W_r < 300$ m) as the fundamental period T_0 lies in the IG band. The curve shifts downward with a decrease in the beach slope because the node associated with the resonant runup amplification is formed at a lower frequency for a milder beach slope. The VLF component creates a slight hump around $W_r = 400$ m which indicates the involvement of the reef-flat resonance. The SS component significantly decreases to the reef end at a higher rate for a larger reef width.

The IG component is dominant in the shoreline motion as well in the right plot. The slope of the declining curve becomes much steeper because the high-frequency IG component ($T < 100$ s), which is more susceptible to the reef-flat dissipation, undergoes tremendous amplification through the runup resonance. The SS component is also significantly amplified over the 1/5 slope for a small reef width as the runup resonance

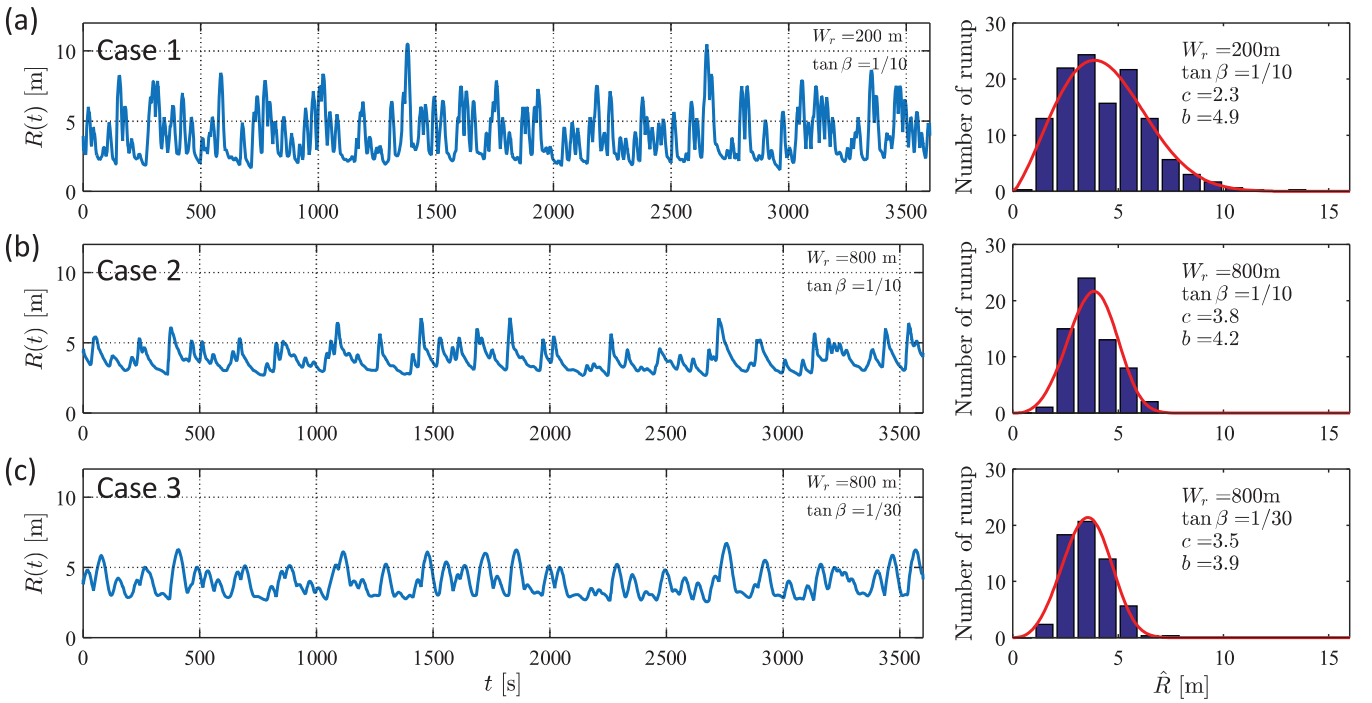

Figure 15. Time series of shoreline elevation and runup histograms for different reef widths and beach slopes computed with H_s=17.3 m and T_p=16.5 s. (a) Case 1: W_r = 200 m and tan β=1/10. (b) Case 2: W_r = 800 m and tan β=1/10. (c) Case 3: W_r = 800 m and tan β=1/30.

period T_R lies in the SS band. The contribution of the reef-flat resonance to the IG runup height seems to be buried in the enhanced high-frequency IG component. The resonant runup amplification produces a large variation of spectral characteristics by the reef width and the beach slope. The combined infragravity wave and sea-swell runup occurs over steep slope beaches fronted by narrow reefs, whereas the low-frequency runup dominates on mild-slope beaches regardless of the reef width.

To clarify the contributions of different physical processes simultaneously involved, we separate the reef friction from the others. Figure 14b represents the same set of results as in Figure 14a, but for the 1/10 beach slope with and without the reef friction. The left plot shows that turning off the friction creates a resonance hump on the curves of the IG and VLF components for narrow reefs (W_r= 100–300 m) and wide reefs (W_r > 300 m), respectively. This is consistent with the fact that the fundamental period shifts from the IG to VLF band around W_r = 300 m. In the actual case with the friction, the reef-flat resonance should enhance the IG and VLF components in the similar manner, though the magnitude is smaller. The IG runup height in the right plot monotonically decreases even without the reef friction implying that a significant amount of wave energy in the high-frequency IG band is dissipated by wave breaking on the reef flat. This is supported by a recent laboratory study which demonstrated that strong dissipation of IG waves by wave breaking takes place in very shallow water [*De Bakker et al.*, 2014].

4.3.2. Flood Characteristics

We finally discuss flood characteristics on the Eastern Samar coast. Figure 15 shows time series of shoreline elevation $R(t)$ for three representative cases: Case 1 (W_r= 200 m and tan β = 1/10), Case 2 (W_r= 800 m and tan β = 1/10), and Case 3 (W_r= 800 m and tan β = 1/30). The time series are plotted for 1 h in the middle of a total computed time of 3 h. Furthermore, corresponding histograms of individual runup heights are graphed in the right plots together with their fitted Weibull distributions. The shape and scale parameters of each distribution defined in equation (8) are displayed in each plot. All the results are computed with the same incident wave profile of H_s=17.3 m and T_p=16.5 s. The two topographic parameters significantly vary along the coastline and thus wave properties differ from site to site accordingly. Although actual beaches on the coast do not have uniform slopes, key characteristics of the coastal flood can be derived from the model results on the simplified topography.

In Case 1 with the narrow reef and steep beach, flood waves are characterized as a superposition of two dominant spectral components as presented in Figure 15a. The shorter component, which is resonantly amplified over the beach, has a mean period of about 20 s. The longer component has a mean period of about 120 s corresponding the reef-flat resonance period of the fundamental mode. High runup occurs when the two components are positively superposed. The sharp wave crest reaches over 10 m above the mean sea level, which occurs a few times per hour. The runup histogram has a broad distribution because of the strong coupling of the two components and the shape factor is close to two meaning that the individual runup heights follow the Rayleigh distribution. During the field survey, some local witnesses at corresponding sites claimed that the maximum water level resulted from multiple waves with short intervals (mostly, three waves). On the ground level of 3–5 m above the mean sea level, where coastal villages are often located, the inundation occurs intermittently when crests of the longer component arrive on the shore. The relationship between the two mean periods of the different components suggests that a single crest of the longer wave accommodates three shorter waves on average. The occurrence of the multiple waves can, therefore, be explained by the superposition of the two spectral components, respectively, enhanced by the two resonance phenomena.

In Case 2 and 3 with the wide reef, the SS component is attenuated by the wave breaking and bottom friction on the reef flat as shown in Figures 15b and 15c. The IG component is also subject to dissipation, but at a smaller rate, and thus the longer wave components become dominant in flood waves. In Case 2 with the steep beach, the IG waves form a bore-like front due to nonlinear steepening, which is called the bore-like surfbeat by *Nakaza and Hino* [1991] who found the phenomenon could occur on the reef coast under severe storm conditions. The bores with different front heights climb up the slope at periods of 100–200 s. On the other hand, the bore-like front does not appear in Case 3 because of strong wave-breaking dissipation over the mild beach (Figure 15c). The resulting flood waves are characterized by a gradual water rise and recession at the similar period as the bore runup in Case 2. The maximum runup is about 6–7 m high and a similar height is reached several times per hour in the both cases. It is also commonly observed that the wide reef flat decreases the number of individual runup waves and makes the runup histogram narrower and more peaked.

Although the runup histograms are similar in Case 2 and 3, flood impacts on the coast could be different as the bore-like wave produces a shock force on structures and houses. Hence, the coastal villages on a typical ground elevation (3–5 m) fronted by a steep beach intermittently suffer from the bore runup at longer intervals. A typical case occurred at the town of Hernani (Pt. 23–25) that was fronted by a 600–700 m wide reef. One of the bore-like waves was captured in the video footage at the town. Local interviews conducted by the authors revealed that similar waves came repeatedly and the one captured in the video was not the largest. On the Pacific coast of Guiuan (Pt. 7–11), where a vast coastal plain extends behind a wide reef of 600–800 m, coastal villages appeared to be inundated by long waves just as in Case 3. Clear watermark lines were found on walls of some buildings, which were rare throughout our survey, indicating that a smooth water surface gradually rose and receded without short waves on it. Damages on inundated houses were relatively minor at the site in spite of an extensive inundation area.

5. Conclusions

Extreme waves generated by super typhoon Haiyan attacked the Eastern Samar coast causing destructive damages to coastal villages. Our postevent field survey revealed that the maximum overwash heights along the southeastern part of the coast varied from 6 to 14 m depending on the reef width and the beach topography behind them. The storm surge simulation based on a parametric typhoon model suggested that the storm surge was not the major cause of the damages on the coast. The significant wave height off the southeastern coast was estimated by WAM at 16–20 m during the most intense period of the storm, decreasing from south to north. The huge waves propagated to the reef front and lost a large portion of their energy through wave breaking and subsequent frictional dissipation on the reef surface. The computed maximum runup heights agree well with the field results when the wave friction factor was set to be around 0.04, which fell in the range of the values estimated by the existing friction formula of the rough turbulence regime. The computed wave setup on the reef flat was 2.2–2.8 m, increasing slightly with reef width.

The flood waves on the shore have a broad spectrum ranging from the SS to VLF band. The SS component is remarkable only on narrow reefs due to strong dissipation by wave breaking and friction on the reef flat and is intensified through resonant runup amplification on steep beaches. The IG component is enhanced at the reef front through nonlinear energy transfer and is also subject to the reef-flat dissipation especially when the reef width is large. The reef-flat resonance of the fundamental mode enhances the low-frequency IG component on narrow reefs and the VLF component on wide reefs although the effect is suppressed by high friction. The contribution of higher-order resonances is not clearly confirmed as their occurrence frequencies overlap with that of the runup resonance on the shore. The high-frequency IG component dominantly contributes to the shoreline motion through resonant runup amplification and rapidly decreases with increasing reef primarily by wave-breaking dissipation. Consequently, the runup height monotonically decreases with increasing reef width and becomes larger on steeper slopes in the range of narrow reef widths because of the contribution of the SS component.

The balance of the different spectral components changes with the reef width and the beach slope to make variations in flood characteristics at different sites. On a steep beach with a narrow reef of a few hundred meters width, two dominant spectral components, respectively, enhanced by the reef-flat and runup resonances are strongly coupled to produce extreme runup heights over 10 m above mean sea level. Flood waves on the higher ground appear as multiple waves that intermittently arrive at the mean period of the longer component. On shores fronted by wide reefs of many hundreds of meters, the bore-like IG waves are formed through nonlinear steepening over steep slope beaches. In places where a coastal plain extends behind a wide reef flat, coastal flooding occurs by a gradual water rise and recession repeated at the period of 100–200 s. The variation of flood characteristics derived from the numerical simulation explains the observed impacts at different sites during the field survey. Further studies are, however, required to fully describe the phenomena, considering two-dimensional wave deformation on actual coastal topography.

Appendix A: Numerical Scheme

For convenience of presenting the numerical method, equations (2)–(6) are rewritten in a compact form as

$$U_t + F_x = S, \tag{A1}$$

where U, F, and S are vectors given by

$$U = \begin{bmatrix} d \\ du \end{bmatrix}, \quad F = \begin{bmatrix} du \\ du^2 + gd^2/2 \end{bmatrix}, \quad S = \begin{bmatrix} 0 \\ -gdz_{bx} - f_w|u|u/2 + \chi \end{bmatrix}, \tag{A2}$$

where,

$$\chi = \gamma d^2 \Gamma_{0xx} + \left(\frac{d^3}{3}\Gamma_1 - \frac{d^2}{2}\Gamma_2\right)_x + z_{bx}\left(\frac{d^2}{2}\Gamma_1 - d\Gamma_2\right). \tag{A3}$$

First, the equation (A1) is discretized by finite differences on a regular grid in space and time. A high-order finite difference scheme similar to those by *Wei and Kirby* [1995] and *Wei et al*. [1995] is chosen as the base scheme. Although it was originally developed for different forms of the Boussinesq-type equation, the robust scheme can also be applied to the present governing equations. The Adams-Bashforth-Moulton method is used for time integration, while the fourth-order operators are employed for spatial differences. The overall scheme is fourth-order accurate and thus free from numerical dispersion due to third-order truncation terms.

The characteristics-based dissipation term is constructed on the basis of the homogeneous part of the equation (A1) and applied at the end of the predictor-corrector step. Let $\hat{U}^{n+1}$ be the numerical solution of the base scheme, the solution at the new time step is calculated by the finite difference equation written in a conservative form,

$$U_i^{n+1}=\hat{U}_i^{n+1}+\frac{\Delta t}{\Delta x}(F^*_{i+1/2}-F^*_{i-1/2}), \tag{A4}$$

where Δt and Δx are the time step and the grid spacing in x-direction, respectively, U_i^n is a discrete approximation of U at $x=i\Delta x$ and $t=n\Delta t$, $F^*_{i+1/2}$ is the dissipative numerical flux defined at the cell center. The terms responsible for the nonlinear dissipation of many shock-capturing methods can be recast in the form of the second term on the right-hand side of the equation. The expression for $F^*_{i+1/2}$ is different depending on the type of shock-capturing methods employed. For the case of the Roe-Sweby TVD scheme, the numerical flux is written as

$$F^*_{i+1/2}=\frac{1}{2}P_{i+1/2}\Phi_{i+1/2}. \tag{A5}$$

Here $P_{i+1/2}$ is the right eigenvector matrix of the Jacobian matrix $\partial F/\partial U$ evaluated by an approximate Riemann solver such as *Roe*'s [1981]. The mth element of the vector $\Phi_{i+1/2}$ denoted by $\phi^m_{i+1/2}$ is written as

$$\phi^m_{i+1/2}=-\left[\left[1-\delta(r^m_{i+1/2})\right]\psi(a^m_{i+1/2})+\delta(r^m_{i+1/2})\lambda(a^m_{i+1/2})^2\right]\alpha^m_{i+1/2}, \tag{A6}$$

where $\lambda=\Delta t/\Delta x$, $a^m_{i+1/2}$ with $m=1, 2$ are the characteristic speeds, which are the eigen values of $\partial F/\partial U$ evaluated using the approximate Riemann solver, $\alpha^m_{i+1/2}$ is the mth element of the characteristic variables calculated by $P^{-1}_{i+1/2}(U_{j+1}-U_j)$, ψ is the entropy correction function to avoid nonphysical solutions,

$$\psi(z)=\begin{cases}|z| & |z|\geq\varepsilon\\ (z^2+\varepsilon^2)/2\varepsilon & |z|<\varepsilon,\end{cases} \tag{A7}$$

and δ is the flux limiter function of the smoothness indicator $r^m_{i+1/2}$ defined by

$$r^m_{i+1/2}=\frac{\alpha^m_{i+1+\sigma}-\alpha^m_{i+\sigma}}{\alpha^m_{i+1}-\alpha_i{}^m}, \quad \sigma=\mathrm{sgn}(a^m_{i+1/2}), \tag{A8}$$

which prevents generation of spurious oscillations in numerical solutions. The solution corresponds to that of the second-order TVD scheme if the flux limiter is chosen in the admissible limiter region by *Sweby* [1984]. Also, the numerical scheme becomes equivalent to the Roe's flux difference splitting scheme if δ is taken to be zero. The characteristic variables α_i^m in equations (A6) and (A8) are evaluated using the source balancing technique by *Rogers et al*. [2003] to avoid the numerical dissipation to be introduced by discontinuous bed slopes.

In order to provide an on/off control of the characteristic-based filter, the switching function is introduced to replace $\Phi_{i+1/2}$ in equation (A5) by

$$\Phi^*_{i+1/2}=\mathrm{diag}(\theta^m_{i+1/2})\Phi_{i+1/2}, \tag{A9}$$

where $\theta^m_{i+1/2}$ is the switching function for $\phi^m_{i+1/2}$ and $\mathrm{diag}(\theta^m_{i+1/2})$ denotes a diagonal matrix with diagonal elements $\theta^m_{i+1/2}$. The function is problem dependent and it is presently aimed at avoiding nonphysical attenuation of prebreaking waves.

Acknowledgments

We would like to thank E. Cruz of University of the Philippines-Diliman and members of Philippine Institute of Civil Engineers for their support on the field work. T.S., Y.T., and S.S. were funded by MEXT through GRENE-City grant program. A.B.K. was funded by the National Science Foundation under grants 1426445 and 1435007. J.S. was funded by JSPS through KAKENHI grant 25303016. The survey data are available in supporting information Table S1 of the supporting information. The best track data of Typhoon Haiyan are available from Digital Typhoon Database (http://agora.ex.nii.ac.jp/digital-typhoon/summary/wnp/l/201330.html.en). The topographic and bathymetric data of the study area are available on the ASTER GDEM (http://www.jspacesystems.or.jp/ersdac/GDEM/E/index.html) and the GEBCO (https://www.bodc.ac.uk/data/online_delivery/gebco/) websites, respectively. The experimental data by *Demirbilek et al*. [2007] were obtained from the CIRP website (http://cirp.usace.army.mil/pubs/). Other data will be made available upon request to the corresponding author (shimozono@coastal.t.u-tokyo.ac.jp).

References

Battjes, J. A., and J. P. F. M. Janssen (1978), Energy loss and set-up due to breaking of random waves, in *Proceedings of 16th International Conference on Coastal Engineering*, pp. 569–587, American Society of Civil Engineers (ASCE), N. Y.

Cheung, K. F., Y. Bai, and Y. Yamazaki (2013), Surges around the Hawaiian Islands from the 2011 Tohoku tsunami, *J. Geophys. Res. Oceans*, *118*, 5703–5719, doi:10.1002/jgrc.20413.

De Bakker, A. T. M., M. F. S. Tissier, and B. G. Ruessink (2014), Shoreline dissipation of infragravity waves, *Cont. Shelf Res.*, *72*, 73–82.

Demirbilek, Z., O. Nwogu, and D. Ward (2007), Laboratory study of wind effect on runup over fringing reefs, *Data Rep. ERDC/CHL-TR-07-4*, U.S. Army Eng. Res. and Dev. Cent. Vicksburg, Miss.

Falter, J. L., M. J. Atkinson, and M. A. Merrifield (2004), Masstransfer limitation of nutrient uptake by a wavedominated reef flat community, *Limnol. Oceanogr. Methods*, *49*(5), 1820–1831.

Gerritsen, F. (1980), Wave attenuation and wave set-up on a coastal reef, in *Proceedings of 17th International Conference on Coastal Engineering*, vol. 1, pp. 444–461, American Society of Civil Engineers (ASCE), N. Y.

Gourlay, M. R. (1994), Wave transformation on a coral-reef, *Coastal Eng.*, *23*(1-2), 161–193.

Gourlay, M. R. (1996a), Wave set-up on coral reefs. 1. Set-up and wave-generated flow on an idealised two dimensional horizontal reef, *Coastal Eng.*, *27*(3-4), 17–42.

Gourlay, M. R. (1996b), Wave set-up on coral reefs. 2. Set-up on reefs with various profiles, *Coastal Eng.*, *28*(1-4), 17–55.

Grüne, J. (2005), Evaluation of wave climate parameters from benchmarking flotsam levels, paper presented at International Conference on Coastlines, Structures and Breakwaters, Inst. of Civ. Eng. London, U. K.
Hardy, T., and I. Young (1996), Field study of wave attenuation on an offshore coral reef, *J. Geophys. Res.*, *101*(C6), 14,311–14,326.
Hearn, C. J. (1999), Wave-breaking hydrodynamics within coral reef systems and the effect of changing relative sea level, *J. Geophys. Res.*, *104*(C12), 30,007–30,019, doi:10.1029/1999JC900262.
IOC, IHO, and BODC (2003), *Centenary Edition of the GEBCO Digital Atlas* [CD-ROM], Br. Oceanogr. Data Cent., Liverpool, U. K.
Jaffe, B., and B. Richmond (1993), Overwash variability on the shoreline of Guam during Typhoon Russ, in *Proceedings of 7th International Coral Reef Symposium*, vol. 1, pp. 257–264. University of Guam Press, UOG Station, Guam.
Jonsson, I. G. (1966), Wave boundary layers and friction factors, in *Proceedings of 10th International Conference on Coastal Engineering*, pp. 127–148, American Society of Civil Engineers (ASCE), N. Y.
Kato, F. (2005), Study on risk assessment of storm surge flood, *Tech. Note* 275, pp. 1–18, Natl. Inst. for Land and Infrastruct. Manage., Tsukuba, Japan.
LeBlond, P. H., S. M. Calisal, and M. Isaacson (1982), Wave spectra in Canadian waters, Canadian contractor report of Hydrography and Ocean Sciences, *Rep. 6*, pp. 193. Marine Environmental Data Services Branch, Department of Fisheries and Oceans, Ottawa, Ontario.
Lowe, R. J., J. L. Falter, M. D. Bandet, G. Pawlak, M. J. Atkinson, S. G. Monismith, and J. R. Koseff (2005), Spectral wave dissipation over a barrier reef, *J. Geophys. Res.*, *110*, C04001, doi:10.1029/2004JC002711.
Lugo-Fernández, A., H. H. Roberts, W. J. Wiseman Jr., and B. L. Carter (1998), Water level and currents of tidal and infragravity periods at Tague Reef, St. Croix (USVI), *Coral Reefs*, *17*(4), 343–349, doi:10.1007/s003380050137.
Madsen, O. S. (1994), Spectral wave-current bottom boundary layer flows, in *Proceedings of 24th International Conference on Coastal Engineering*, pp. 384–398, American Society of Civil Engineers (ASCE), N. Y.
Madsen, P. A., R. Murray, and O. R. Sorensen (1991), A new form of the Boussinesq equations with improved linear dispersion characteristics, *Coastal Eng.*, *15*(4), 371–388.
Mas, E., J. Bricker, S. Kure, B. Adriano, C. Yi, A. Suppasri, and S. Koshimura (2014), Field survey report and satellite image interpretation of the 2013 Super Typhoon Haiyan in the Philippines, *Nat. Hazards Earth Syst. Sci.*, *2*, 3741–3767.
Mase, H., and Y. Iwagaki (1984), Run-up of random waves on gentle slopes, in *Proceedings of 19th International Conference on Coastal Engineering*, vol. 19, pp. 593–609, American Society of Civil Engineers (ASCE), N. Y.
Massel, S. R., and M. R. Gourlay (2000), On the modelling of wave breaking and set-up on coral reefs, *Coastal Eng.*, *39*(1), 1–27.
Matsumoto, K., T. Takanezawa, and M. Ooe (2000), Ocean tide models developed by assimilating TOPEX/POSEIDON altimeter data into hydrodynamical model: A global model and a regional model around Japan, *J. Oceanogr.*, *56*, 567–581.
Mitsuta, Y., and T. Fujii (1987), Analysis and synthesis of typhoon wind pattern over Japan, *Bull. Disaster Prev. Res. Inst.*, *37*(4), 169–185.
Monismith, S. G. (2007), Hydrodynamics of coral reefs, *Annu. Rev. Fluid Mech.*, *39*(1), 37–55, doi:10.1146/annurev.fluid.38.050304.092125.
Mori, N., M. Kato, S. Kim, H. Mase, Y. Shibutani, T. Takemi, K. Tsuboki, and T. Yasuda (2014), Local amplification of storm surge by Super Typhoon Haiyan in Leyte Gulf, *Geophys. Res. Lett.*, *41*, 5106–5113, doi:10.1002/2014GL060689.
Munk, W. H. (1950), Origin and generation of waves, in *Proceedings of 1st International Conference on Coastal Engineering*, pp. 1–4, American Society of Civil Engineers (ASCE), N. Y.
Myers, V. A. (1954), Characteristics of United States hurricanes pertinent to levee design for Lake Okeechobee, Florida, *Hydrometeorol. Rep.* 32, U.S. Dep. of Commer., Weather Bur., Washington, D. C.
Nakaza, E., and M. Hino (1991), Bore-like surf beat in a reef zone caused by wave groups of incident short period waves, *Fluid Dyn. Res.*, *7*(2), 89–100, doi:10.1016/0169-5983(91)90062-N.
Nakaza, E., S. Tsukayama, and M. Hino (1990). Bore-like surf beat on reef coasts, in *Proceeding of 22nd International Conference on Coastal. Engineering*, pp. 743–756, American Society of Civil Engineers (ASCE), N. Y.
Nelson, R. C. (1996), Hydraulic roughness of coral reef platforms, *Appl. Ocean Res.*, *18*(5), 265–274.
Nwogu, O., and Z. Demirbilek (2010), Infragravity wave motions and runup over shallow fringing reefs, *J. Waterway Port Coastal Ocean Eng.*, *136*, 295–305.
Oey, L. Y., T. Ezer, D. P. Wang, S. J. Fan, and X. Q. Yin (2006), Loop current warming by Hurricane Wilma, *Geophys. Res. Lett.*, *33*, L08613, doi:10.1029/2006GL025873.
Ogg, J., and J. Koslow (1978), The impact of typhoon Pamela (1976) on Guams coral reefs and beaches, *Pac. Sci.*, *32*(2), 105–118.
Ohyama, T., and K. Nadaoka (1991), Development of a numerical wave tank for analysis of nonlinear and irregular wave field, *Fluid Dyn. Res.*, *8*, 231–251.
Péquignet, A. C., J. M. Becker, M. A. Merrifield, and J. Aucan (2009), Forcing of resonant modes on a fringing reef during tropical storm Man-Yi, *Geophys. Res. Lett.*, *36*, L03607, doi:10.1029/2008GL036259.
Péquignet, A. C., J. M. Becker, M. A. Merrifield, and S. J. Boc (2011), The dissipation of wind wave energy across a fringing reef at Ipan, Guam, *Coral Reefs*, *30*(S1), 71–82, doi:10.1007/s00338-011-0719-5.
PLAN International Website (2014), Typhoon Haiyan washes house away, PLAN International, Woking, U. K. [Available at http://plan-international.org/about-plan/resources/videos/video-typhoon-washes-house-away/.]
Pomeroy, A., R. Lowe, G. Symonds, A. Van Dongeren, and C. Moore (2012), The dynamics of infragravity wave transformation over a fringing reef, *J. Geophys. Res.*, *117*, C11022, doi:10.1029/2012JC008310.
Ribera, P., R. GarcaHerrera, and L. Gimeno (2008), Historical deadly typhoons in the Philippines, *Weather*, *63*(7), 194–199.
Roe, P. L. (1981), Approximate Riemann solvers, parameter vectors and difference schemes, *J. Comput. Phys.*, *43*(2), 357–372.
Roeber, V., and K. F. Cheung (2012), Boussinesq-type model for energetic breaking waves in fringing reef environments, *Coastal Eng.*, *70*, 1–20.
Roeber, V., Y. Yamazaki, and K. F. Cheung (2010), Resonance and impact of the 2009 Samoa tsunami around Tutuila, American Samoa, *Geophys. Res. Lett.*, *37*, L21604, doi:10.1029/2010GL044419.
Rogers, B. D., A. G. L. Borthwick, and P. H. Taylor (2003), Mathematical balancing of flux gradient and source terms prior to using Roe's approximate Riemann solver, *J. Comput. Phys.*, *192*(2), 422–451.
Seabra-Santos, F. J., D. P. Renouard, and A. M. Temperville (1987), Numerical and experimental study of the transformation of a solitary wave over a shelf or isolated obstacle, *J. Fluid Mech.*, *176*, 117–134.
Sheremet, A., J. M. Kaihatu, S.-F. Su, E. R. Smith, and J. M. Smith (2011), Modeling of nonlinear wave propagation over fringing reefs, *Coastal Eng.*, *58*, 1125–1137.
Skotner, C., and C. J. Apelt (1999), Application of a Boussinesq model for the computation of breaking waves. Part 2: Wave-induced set-down and setup on a submerged coral reef, *Ocean Eng.*, *26*, 927–947.
Stefanakis, T., F. Dias, and D. Dutykh (2011), Local runup amplification by resonant wave interactions, *Phys. Rev. Lett.*, *107*, 124502.

Swart, D. H. (1974), Offshore sediment transport and equilibrium beach profiles, *Tech. Rep*. 131, Delft Hydraul. Lab., Delft, Netherlands.
Sweby, P. K. (1984), High resolution schemes using flux limiters for hyperbolic conservation laws, *SIAM J. Numer. Anal.*, *21*, 995–1011.
Symonds, G., D. A. Huntley, and A. J. Bowen (1982), Two-dimensional surf beat: Long wave generation by a timevarying breakpoint, *J. Geophys. Res.*, *87*(C1), 492–498.
Tajima, Y., et al. (2014), Initial report of JSCE-PICE joint survey on the storm surge disaster caused by typhoon Haiyan, *Coastal Eng. J.*, *56*, 1450006, doi:10.1142/S0578563414500065.
The Wamdi Group (1988), The WAM model—A third generation ocean wave prediction model, *J. Phys. Oceanogr.*, *18*, 1775–1810.
Torres-Freyermuth, A., I. Mario-Tapia, C. Coronado, P. Salles, G. Medelln, A. Pedrozo-Acua, R. Silva, J. Candela, and R. Iglesias-Prieto (2012), Wave-induced extreme water levels in the Puerto Morelos fringing reef lagoon, *Nat. Hazards Earth Syst. Sci.*, *12*, 3765–3773.
UNEP-WCMC, WorldFish Centre, WRI, and TNC (2010), Global distribution of warm-water coral reefs, compiled from multiple sources and including IMaRS-USF and IRD (2005), IMaRS-USF (2005) and Spalding et al. (2001), UNEP World Conserv. Monit. Cent., Cambridge, U. K. [Available at http://data.unep-wcmc.org/ datasets/13.]
Van Dongeren, A., R. Lowe, A. Pomeroy, D. M. Trang, D. Roelvink, G. Symonds, and R. Ranasinghe (2013), Numerical modeling of low-frequency wave dynamics over a fringing coral reef, *Coastal Eng.*, *73*, 178–190.
Wei, G., and J. T. Kirby (1995), Time-dependent numerical code for extended Boussinesq equations, *J. Waterway Port Coastal Ocean Eng.*, *121*(5), 251–261.
Wei, G., J. T. Kirby, S. T. Grilli, and R. Subramanya (1995), A fully nonlinear Boussinesq model for surface waves. Part 1. Highly nonlinear unsteady waves, *J. Fluid Mech.*, *294*(7), 71–92.
Welch, P. D. (1967), The use of Fast Fourier Transform for the estimation of power spectra: A method based on time averaging over short, modified periodograms, *IEEE Trans. Audio Electroacoust.*, *AU-15*, 70–73.
Yee, H. C., N. D. Sandham, and M. J. Djomehri (1999), Low-dissipative high-order shock-capturing methods using characteristic-based filters, *J. Comput. Phys.*, *150*, 199–238.
Young, I. R. (1989), Wave transformation over coral reefs, *J. Geophys. Res.*, *94*(C7), 9779–9789.
Young, J. G., and M. D. Cruz (2002), Eastern Visayas Reefs: Guiuan and adjacent islands, in *Atlas of Philippine Coral Reefs*, edited by P. M. Alio et al., pp. 157–159, Goodwill Trading Co. Inc., Makati, Philippines.
Zijlema, M. (2012), Modelling wave transformation across a fringing reef using SWASH, paper 26 presented at 33rd International Conference on Coastal Engineering, American Society of Civil Engineers (ASCE), N. Y.